RESEARCH ARTICLE

Continuous sensing of IFNα by hepatic endothelial cells shapes a vascular antimetastatic barrier

Ngoc Lan Tran[1†‡], Lorena Maria Ferreira[1†], Blanca Alvarez-Moya[1†], Valentina Buttiglione[1§], Barbara Ferrini[1], Paola Zordan[1,2], Andrea Monestiroli[1], Claudio Fagioli[1], Eugenia Bezzecchi[3], Giulia Maria Scotti[3], Antonio Esposito[2,4], Riccardo Leone[2,4], Chiara Gnasso[2,4], Andrea Brendolan[5], Luca G Guidotti[1,2], Giovanni Sitia[1]*

[1]Division of Immunology, Transplantation and Infectious Diseases, IRCCS San Raffaele Scientific Institute, Milan, Italy; [2]Vita-Salute San Raffaele University, Milan, Italy; [3]Center for Omics Sciences, IRCCS San Raffaele Hospital, Milan, Italy; [4]Experimental Imaging Center, IRCCS San Raffaele Scientific Institute, Milan, Italy; [5]Division of Experimental Oncology, IRCCS San Raffaele Scientific Institute, Milan, Italy

Abstract Hepatic metastases are a poor prognostic factor of colorectal carcinoma (CRC) and new strategies to reduce the risk of liver CRC colonization are highly needed. Herein, we used mouse models of hepatic metastatization to demonstrate that the continuous infusion of therapeutic doses of interferon-alpha (IFNα) controls CRC invasion by acting on hepatic endothelial cells (HECs). Mechanistically, IFNα promoted the development of a vascular antimetastatic niche characterized by liver sinusoidal endothelial cells (LSECs) defenestration extracellular matrix and glycocalyx deposition, thus strengthening the liver vascular barrier impairing CRC trans-sinusoidal migration, without requiring a direct action on tumor cells, hepatic stellate cells, hepatocytes, or liver dendritic cells (DCs), Kupffer cells (KCs) and liver capsular macrophages (LCMs). Moreover, IFNα endowed LSECs with efficient cross-priming potential that, along with the early intravascular tumor burden reduction, supported the generation of antitumor $CD8^+$ T cells and ultimately led to the establishment of a protective long-term memory T cell response. These findings provide a rationale for the use of continuous IFNα therapy in perioperative settings to reduce CRC metastatic spreading to the liver.

Editor's evaluation

This study describing how continuous perioperative IFNα therapy stimulates hepatic endothelial cells to build up a physical vascular barrier that limits tumor cell entry into the liver and promotes long-term antitumor immunity provides novel evidence for anti-metastatic effects of IFNα via effects on the liver vascular compartment. This work is predicted to advance the field and will be of interest to scientists studying cancer, inflammation and liver function.

***For correspondence:** sitia.giovanni@hsr.it

[†]These authors contributed equally to this work

Present address: [‡]University of Geneva, Geneva, Switzerland; [§]Ipsen Spa, Assago, Italy

Competing interest: See page 28

Funding: See page 28

Preprinted: 11 May 2022
Received: 01 June 2022
Accepted: 18 September 2022
Published: 25 October 2022

Reviewing Editor: Victoria L Bautch, University of North Carolina, Chapel Hill, United States

© Copyright Tran, Ferreira, Alvarez-Moya *et al*. This article is distributed under the terms of the Creative Commons Attribution License, which permits unrestricted use and redistribution provided that the original author and source are credited.

Introduction

Colorectal cancer (CRC) is the third most common cancer and the second leading cause of cancer-related death worldwide (***Sung et al., 2021***). Surgical resection of the primary CRC tumor is the mainstay of treatment (***Argilés et al., 2020***; ***Cunningham et al., 2010***; ***Seo et al., 2013***) unfortunately, up to 50% of these patients – despite chemotherapy and targeted adjuvant therapies – often develop life-threatening liver metastatic disease in the following years (***Argilés et al., 2020***; ***Sargent et al.,***

eLife digest Colorectal cancer remains one of the most widespread and deadly cancers worldwide. Poor health outcomes are usually linked to diseased cells spreading from the intestine to create new tumors in the liver or other parts of the body. Treatment involves surgically removing the initial tumors in the bowel, but patient survival could be improved if, in parallel, their immune system was 'boosted' to destroy cancer cells before they can form other tumors.

Interferon alpha is a small protein which helps to coordinate how the immune system recognizes and deactivates foreign agents and cancerous cells. It has recently been trialed as a colorectal cancer treatment to prevent tumors from spreading to the liver, but only with limited success. This partly because interferon-alpha is usually administered in high and pulsed doses, which cause severe side effects through the body.

Instead, Tran, Ferreira, Alvarez-Moya et al. aimed to investigate whether continuously delivering lower amounts of the drug could be a better approach. This strategy was tested on mice in which colorectal cancer cells had been implanted into the wall of the large intestine. Continuous administration minimized the risk of the implanted cancer cells spreading to the liver while also creating fewer side effects. The team was able to identify an optimum delivery strategy by varying how much interferon-alpha the animals received and when.

Further experiments also revealed a new mechanism by which interferon-alpha prevented the spread of colorectal cancer. Upon receiving continuous doses of the drug, a group of liver cells started to generate a physical barrier which stopped cancer cells from being able to invade the organ. The treatment also promoted long-term immune responses that targeted diseased cells while being safe for healthy tissues. If confirmed in clinical trials, these results suggest that colorectal patients undergoing tumor removal surgery may benefit from also receiving interferon-alpha through continuous delivery.

2009). While the overall benefit of surgery is well established (***Seo et al., 2013***), it has been also proposed that this procedure may foster liver metastases by increasing the dissemination of CRC cells into the portal circulation (***Chow and Chok, 2019***; ***Denève et al., 2013***), enhancing the adhesion of CRC cells to the liver endothelium (***Chambers et al., 2002***; ***Gül et al., 2011***) or promoting transient immunosuppression awakening dormant intrahepatic micrometastases (***Ananth et al., 2016***).

Accordingly, there is growing recognition that the use of perioperative immunotherapies in CRC patients undergoing surgical resection may represent a unique treatment window to prevent metastatic colonization and control minimal residual disease (***Badia-Ramentol et al., 2021***; ***Bakos et al., 2018***; ***Horowitz et al., 2015***). In this context, interferon-alpha (IFNα), a pleiotropic cytokine with multiple antitumor effects such as the direct inhibition of cancer cell growth and angiogenesis (***Indraccolo, 2010***), the sustained upregulation of major histocompatibility complexes (***Gessani et al., 2014***) and the induction of innate and adaptive antitumor immune responses (***Aichele et al., 2006***; ***Curtsinger et al., 2007***; ***Fuertes et al., 2013***), has been used as adjuvant immunotherapy in various solid cancers such as renal cell carcinoma (***Flanigan et al., 2001***), melanoma (***Lens and Dawes, 2002***) and colorectal cancer (***Köhne et al., 1997***; ***Link et al., 2005***). Unfortunately, systemic administration of IFNα has shown limited clinical efficacy, likely due to its short plasma half-life (~1 hr) (***Bocci, 1994***) and the use of high and pulsed doses, which often resulted in systemic side effects (***Weber et al., 2015***). To overcome these limitations, several strategies to prolong IFNα half-life and target the tumor microenvironment have been tested (***Fioravanti et al., 2011***; ***Herndon et al., 2012***; ***Jeon et al., 2013***; ***Li et al., 2017***; ***Liang et al., 2018***; ***Yang et al., 2014***), including a preclinical gene/cell therapy approach that can deliver constant amounts of IFNα into the liver to significantly curb CRC metastatic growth (***Catarinella et al., 2016***).

Herein, we adopted a continuous intraperitoneal (ip) IFNα delivery strategy to show that steady and tolerable IFNα doses reduce liver CRC metastatic spreading and improves survival in several CRC mouse models. Our results showed that the antimetastatic effects of IFNα rely neither on the direct inhibition of tumor cell proliferation nor on the indirect stimulation of hepatocytes, hepatic stellate cells, liver DCs, Kupffer cells (KCs) and liver capsular macrophages (LCMs). Rather, the results identify HECs, including LSECs, as key mediators of IFNα-dependent anti-tumor activities that involve the

impairment of CRC trans-sinusoidal migration and the development of long-term anti-tumor CD8⁺ T cell immunity.

Results

Selection of the optimal IFNα dosing regimen

To avoid well-known toxicities, especially myelotoxicity, caused by high IFNα doses (***Weber et al., 2015***) and to define a delivery strategy providing prolonged and non-fluctuating IFNα levels in blood and tissues, normal inbred mice were implanted intraperitoneally with mini-osmotic pumps (MOP) constantly releasing different rates (i.e. 50 ng/day, 150 ng/day, or 1050 ng/day) of recombinant mouse IFNα1 (termed IFNα from now on) over time. Serum IFNα levels peaked at day 2 after MOP implantation and relative IFNα amounts (from ~100 pg/ml to ~1200 pg/ml) reflected the different MOP loading doses (***Figure 1A***). Serum IFNα levels decreased, albeit not uniformly, at days 5 and 7 post implantation (***Figure 1A***), mirroring the pharmacokinetic-pharmacodynamic (PK-PD) behavior of other long-lasting formulations of IFNα (***Jeon et al., 2013***). A reduction in circulating white blood cells (WBCs) but not in platelet (PLT) counts or hematocrit (HCT) was detected only with the highest dose (***Figure 1B*** and ***Figure 1—figure supplement 1A,B***). Looking at liver toxicity, we observed no increases in serum alanine aminotransferase (sALT) at all tested doses and time points (***Figure 1—figure supplement 1C***) and no abnormal changes in liver morphology at autopsy (***Figure 1—figure supplement 1D***). Looking at the intrahepatic induction of the interferon-stimulated gene (ISG) *Irf7* (***Cheon et al., 2014***) at day 7, we observed a proportional dose response, with a six-fold increase in *Irf7* expression at the 150 ng/day dosing regimen (***Figure 1C***). Notably, this increase paralleled the increase that we previously documented to be associated with protection against liver CRC colonization following a gene/cell therapy based IFNα delivery strategy (***Catarinella et al., 2016***). Lack of bone marrow and liver toxicity, proper induction of hepatic *Irf7* expression and maintained responsiveness of hepatic liver cells to IFNα (***Figure 1—figure supplement 1E***) prompted us to select the 150 ng/day dosing regimen for follow-up investigations.

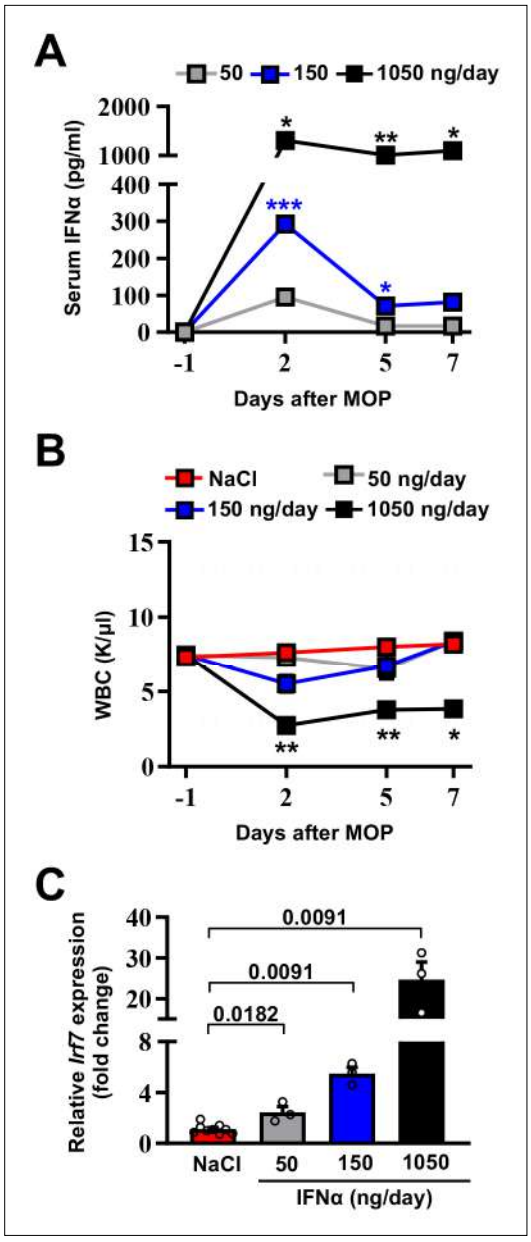

Figure 1. Selection of the optimal IFNα dosing regimen. (**A**) Quantification of plasma IFNα concentration from mice continuously treated with different IFNα doses at the indicated time points. Mean values ± SEM are shown; p-values were calculated by one-way ANOVA Tukey's multiple comparison test. Significant p-values refer to the IFNα 50 ng/day group, since NaCl-treated animals had IFNα plasma levels below the assay detection limit. p≤0.05; **p≤0.01; ***p≤0.001. (**B**) White blood cell (WBC) counts of mice treated with different IFNα doses at indicated time points. Horizontal dashed lines delimit normal WBC range. Mean value ± SEM are shown; p-values were calculated by one-way ANOVA Tukey's multiple comparison test. Significant p-values are referred to the NaCl group. *p≤0.05; **p≤0.01. (**C**) Quantitative real-time PCR analysis of *Irf7* mRNA expression from

Figure 1 continued on next page

Figure 1 continued

liver tissues of mice treated with different IFNα doses for 7 days. Basal *Irf7* mRNA expression level was determined in control mice (NaCl; n=9) and the relative expression of *Irf7* upon IFNα treatment is shown (n=3, for each IFNα-treated group). Mean values ± SEM are shown; p-values were calculated by Mann-Whitney test.

The online version of this article includes the following source data and figure supplement(s) for figure 1:

Source data 1. Data for the dose-response curves in the figure.

Figure supplement 1. Selection of the optimal IFNα dosing regimen.

Figure supplement 1—source data 1. Data for the dose-response curves in the figure.

Continuous IFNα administration reduces liver CRC metastatic burden and improves survival

We next tested the ability of continuous IFNα administration (150 ng/day for 28 days) to reduce CRC metastatic growth in the liver. Groups of H-2^{bxd} F1 hybrids of C57BL/6 J x BALB/c (CB6) mice were implanted with either control MOP-NaCl (termed NaCl) or MOP-IFNα (termed IFNα) (***Figure 2A***). Seven days later, a time frame compatible with the perioperative period in humans (***Horowitz et al., 2015***), CB6 mice were intrasplenically challenged with either the immunogenic microsatellite instable (MSI) MC38 CRC cell line (***Efremova et al., 2018***; ***Rosenberg et al., 1986***) or the poorly immunogenic microsatellite stable (MSS) CT26 CRC cell line (***Brattain et al., 1980***; ***Efremova et al., 2018***). Rapid removal of the spleen after CRC cell injection was implemented to avoid intrasplenic tumor growth (***Catarinella et al., 2016***). Each CRC cell line was injected at doses known to induce similar survival rates in age- and sex-matched CB6 recipients that, carrying hybrid H-2^{bxd} alleles, are immunologically permissive to both MC38 and CT26 cells (***Catarinella et al., 2016***). After treatment initiation, well-tolerated serum IFNα levels of ~300 pg/ml at day 2 and ~100 pg/ml thereafter were observed (***Figure 2B*** and ***Figure 2—figure supplement 1A,B***), which subsequently declined to undetectable levels. The intrahepatic expression of *Irf7* monitored at day 21 after continuous IFNα therapy (***Figure 2—figure supplement 1C, D***) was like that observed earlier at day 7 (***Figure 1C***). Magnetic resonance imaging (MRI)-based longitudinal analyses – in MC38- (***Figure 2C*** and ***Figure 2—figure supplement 1E***) or CT26-challenged (***Figure 2D*** and ***Figure 2—figure supplement 1F***) animals – revealed that 100% of NaCl-treated mice (***Figure 2E and F***) develop multiple metastatic tumor lesions by days 21 and 28 after challenge and no mice displayed detectable tumors in other organs. Liver lesions increased in volume afterwards, ultimately resulting in imposed humane euthanization of both MC38 (***Figure 2—figure supplement 1I***) or CT26 (***Figure 2—figure supplement 1J***) tumor carriers in the intervening weeks. Conversely, 45% and 66% of IFNα-treated mice challenged with MC38 or CT26 cells, respectively, showed absence of liver metastases throughout the entire duration of the experiment (***Figure 2E and F***). All the remaining mice scoring disease-positive at days 21 and 28 displayed lesions that were reduced in number and size when compared to those detected in NaCl-treated counterparts (***Figure 2—figure supplement 1G, J***). Of note, metastatic lesions eventually regressed and achieved complete remission by day 50 in approximately 33% of IFNα-treated mice that were challenged with MC38 cells and scored disease-positive at day 21 (***Figure 2C and E*** and ***Figure 2—figure supplement 1E***), whereas none of the few CT26-challenged mice scoring disease-positive at day 21 survived long-term (***Figure 2D and F*** and ***Figure 2—figure supplement 1F***), with tumors confined only to the liver. Continuous IFNα administration also improved survival, with similar rates for both MC38- and CT26-challenged mice (***Figure 2G and H***). These results indicate that the continuous IFNα administration safely and efficiently limits the liver metastatic colonization of CRC cell lines intrinsically carrying different immunogenic or genetic properties.

Continuous IFNα administration prevents spontaneous hepatic colonization of orthotopically implanted CT26^{LM3} cells

To confirm the above-mentioned results in a different metastatic setting, we developed an orthotopic CRC model of liver metastases by implanting invasive CRC cells into the mouse cecal wall. As previously reported (***Zhang et al., 2013***), invasive CRC cells were generated by serial intracecal injections of the parental CT26 cells into CB6 mice (***Figure 3—figure supplement 1A***). The percentage of metastatic livers in intracecally implanted mice significantly increased as CT26 cells were passaged, with an almost 100% of animals bearing multiple liver metastases after 3 rounds of in vivo selection

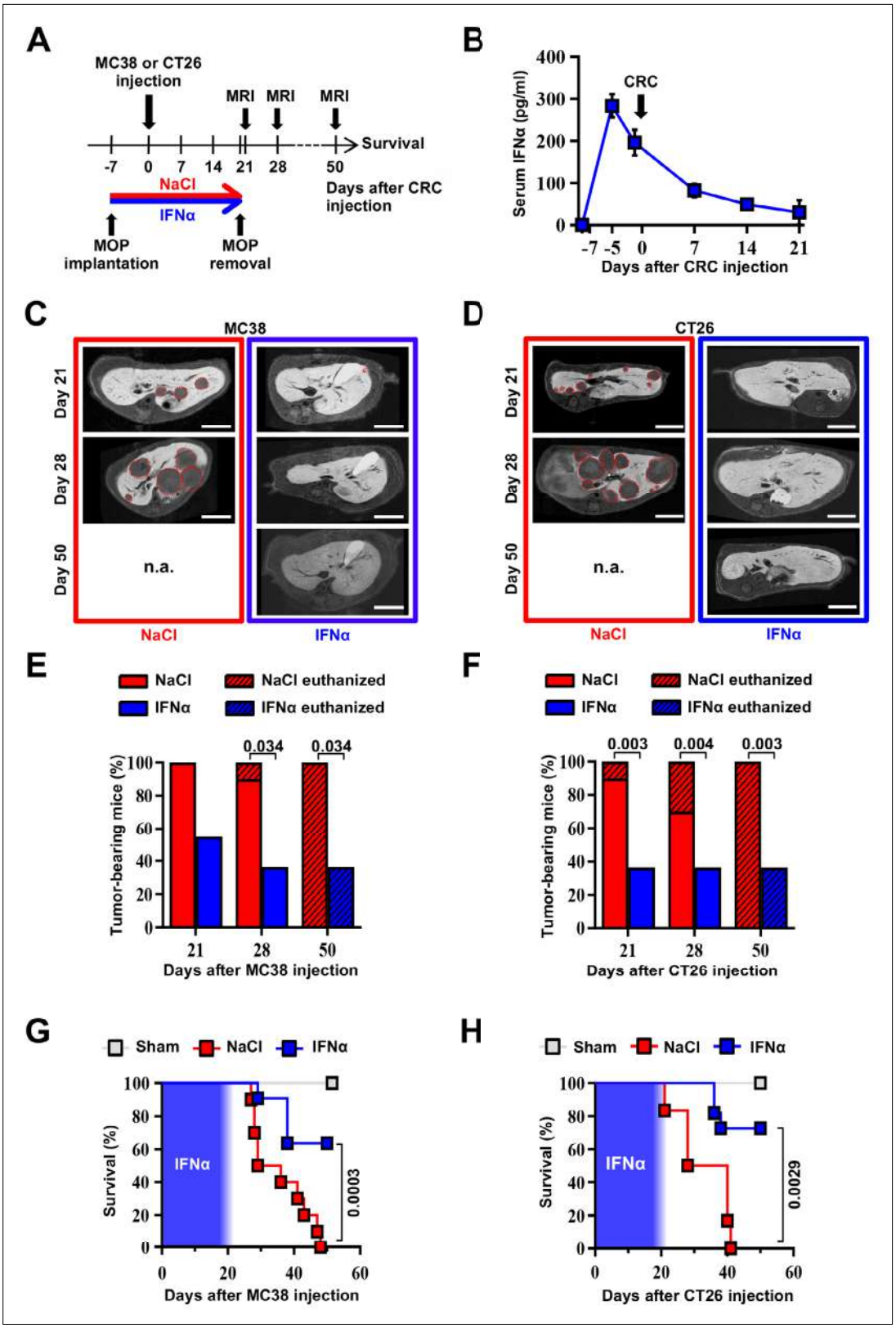

Figure 2. Continuous IFNα administration reduces liver CRC metastatic burden and improves survival. (**A**) Schematic representation of the experimental procedure. Intrasplenic injection of $7x10^4$ MC38 or $5x10^3$ CT26 cells was performed 7 days after continuous NaCl or IFNα therapy. (**B**) Quantification of plasma IFNα concentration at different time points after continuous IFNα administration (n=6). The time of intrasplenic CRC cell injection has also been depicted. Mean values ± SEM are shown. (**C–D**) Representative T1 contrast-enhanced magnetic resonance images (MRI) of the liver of mice treated

Figure 2 continued on next page

Figure 2 continued

with NaCl (red frame) and IFNα (blue frame) at 21, 28, and 50 days after MC38 (**C**) or CT26 (**D**) cells injection. Red dashed lines highlight CRC liver metastases, characterized as hypointense regions in T1-weighted sequences. n.a.=not assessed, is referred to mice euthanized before the specified time point; scale bar = 5 mm. (**E–F**) Percentage of mice treated with NaCl (MC38 n=3 + 3; CT26 n=5 + 5 for each of two independent experiments) or IFNα (MC38 n=5 + 6; CT26 n=5 + 6 for each of two independent experiments) bearing at least one CRC liver metastasis estimated by MRI analysis at indicated time points after MC38 or CT26 injection. The oblique black line pattern within columns depicts the percentage of mice euthanized before the indicated time point. Mean values are shown; p-values were calculated by Fisher's exact test. (**G–H**) Kaplan-Meier survival curves of Sham (n=3), NaCl- (MC38 n=6; CT26 n=10) or IFNα-treated (MC38 n=11; CT26 n=11) mice after MC38 or CT26 cells injection. The blue pattern indicates the time frame of IFNα ip release; p-values were calculated by log-rank/Mantel-Cox test.

The online version of this article includes the following source data and figure supplement(s) for figure 2:

Source data 1. Data for the graphs in the figure.

Figure supplement 1. Continuous intraperitoneal IFNα administration reduces MC38 and CT26 metastatic tumor burden without causing significant hematologic toxicity.

Figure supplement 1—source data 1. Data for the graphs in the figure.

(***Figure 3—figure supplement 1B-D***). Three-time passaged cells (termed $CT26^{LM3}$) were then orthotopically implanted in the cecal wall of CB6 mice and 7 days later the animals were treated with either NaCl or IFNα (***Figure 3A***).

Consistent with our previous results (***Figure 2B***), serum IFNα levels peaked at day 2 after MOP implantation (***Figure 3B***), without causing myelotoxicity (***Figure 3C***), and MRI analyses performed 14 days later revealed that continuous IFNα therapy did not alter the growth of primary intracecal tumors (***Figure 3D and E***), while IFNα treatment significantly reduced both number and size of hepatic lesions (***Figure 3D and F***) with 60% of mice spared from metastatic lesions (***Figure 3H***). The primary intracecal tumors (***Figure 3—figure supplement 2A***) and liver metastases (***Figure 3G***) detected after orthotopic implantation of $CT26^{LM3}$ cells were also characterized by immunohistochemistry (IHC). This analysis showed that primary intracecal tumors and liver metastatic lesions of NaCl-treated control mice were highly proliferative (as denoted by Ki67 positivity), exhibited marked signs of angiogenesis (as denoted by CD34 staining) and, accordingly with previous reports (***Catarinella et al., 2016***; ***Tauriello et al., 2018***), were devoted of $F4/80^+$ resident macrophages and $CD3^+$ T cells (***Figure 3G and H***). Similar results were also observed in IFNα-treated primary intracecal tumors (***Figure 3—figure supplement 2A, B***). The absence of liver metastases in the majority of IFNα-treated mice is reflected by a reduced Ki67 or CD34 staining and an apparently normal distribution of $F4/80^+$ macrophages and $CD3^+$ T cells (***Figure 3G and H***). The few small hepatic lesions detected in 40% of mice continuously treated with IFNα (***Figure 3H*** and ***Figure 3—figure supplement 2C, D***) did not show differences in Ki67 positivity, CD34 staining or amount of $F4/80^+$ resident macrophages and $CD3^+$ T cells in relation to NaCl-treated mice (***Figure 3—figure supplement 2C, D***), consistent with the notion that CRC tumors may deregulate the *Ifnar1* receptor and, thus, become refractory to IFNα therapy (***Boukhaled et al., 2021***; ***Katlinski et al., 2017***).

Altogether, these results indicate that continuous IFNα therapy does not significantly alter the growth of primary established CRC tumors but reduces the liver metastatic potential of invasive CRC cells emerging from the cecum.

HECs mediate the anti-metastatic activity of IFNα

As the *Ifnar1* surface receptor subunit is necessary to mediate the pleiotropic anti-tumor properties of IFNα (***Cheon et al., 2014***), we deleted this molecule from CRC cells and from hepatic parenchymal and non-parenchymal cells to identify the mechanism of action (MoA) of continuous IFNα administration in our in vivo system. We restricted these studies to MC38 CRC cells because the genetic background of the mouse models did not allow us to use CT26 CRC MHC-I mismatched cell lines in C57BL/6 recipients. We also adopted a new seeding approach that – involving the injection of CRC cells through the superior mesenteric vein – potentially avoids immune deregulations linked to the splenectomy procedure. Seven days after NaCl or IFNα administration, C57BL/6 mice were challenged with wild-type MC38 cells or with MC38 cells that were CRISPR-Cas9-edited to lack a functional *Ifnar1* receptor ($MC38^{Ifnar1_KO}$). To this end, MC38-edited clones showed mismatches in a T7E1 assay and clone C8 ($MC38^{C8}$) carrying *Ifnar1* deleting mutations failed to express *Irf7* upon in vitro IFNα stimulation (***Figure 4—figure supplement 1A-C***).

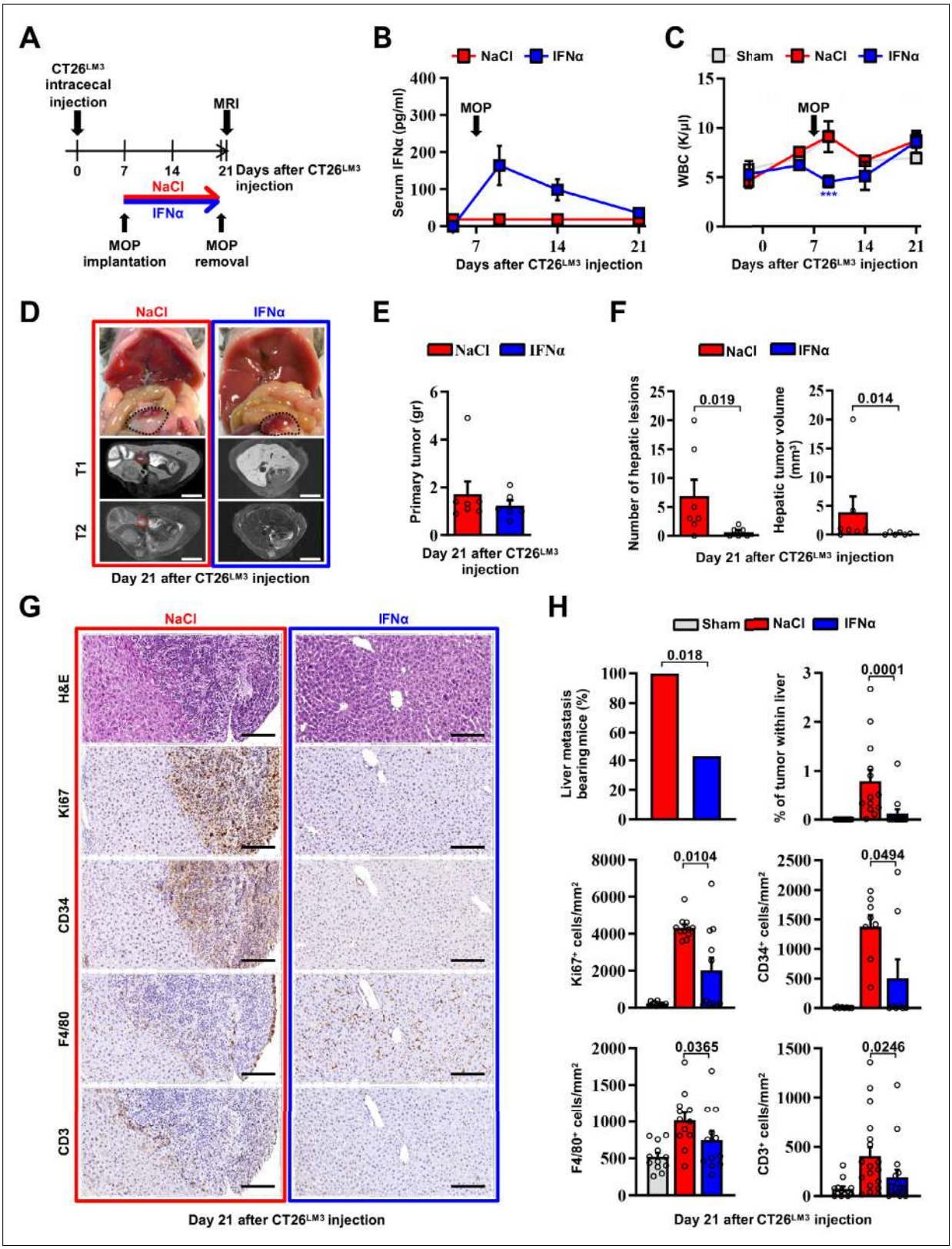

Figure 3. Continuous IFNα administration prevents spontaneous hepatic colonization of orthotopically implanted CT26^{LM3} cells. (**A**) Schematic representation of the experimental procedure. Seven days after intracecal injection of 2x10^5 CT26^{LM3} cells, mice were randomly assigned to receive either continuous NaCl (n=7) or IFNα (n=6) administration and analyzed by MRI 14 days later. (**B**) Quantification of plasma IFNα concentration at the indicated time point after cecal wall injection of CT26^{LM3} cells in mice described in a. The arrow indicates the time of NaCl or IFNα therapy initiation.

Figure 3 continued on next page

Figure 3 continued

Mean values ± SEM are shown. (**C**) WBC counts from mice described in (**A**) continuously treated with NaCl or IFNα at indicated time points. Horizontal dashed lines delimit the normal WBC range. The time of MOP implantation has also been depicted. Mean value ± SEM are shown; p-values were calculated by one-way ANOVA Tukey's multiple comparison test. Significant p-values are referred to NaCl group. ***p≤0.001. (**D**) Representative images (top panels) of the hepatic lesions and intracecal tumors observed in NaCl- (red frame) and IFNα-treated (blue frame) mice, 21 days after $CT26^{LM3}$ cells intracecal wall injection, and the corresponding hepatic contrast-enhanced MRI, T1-weighted (middle panels) and T2-weighted (bottom panels) sequences. Red dashed lines identify macroscopic liver metastatic lesions. Scale bars = 5 mm. (**E**) Quantification of the weight of primary CRC tumors 21 days after $CT26^{LM3}$ cells intracecal wall injection of mice described in D. (**F**) Quantification of the number of hepatic lesions and total tumor volume of liver metastases by MRI analysis of mice described in D. Mean values ± SEM are shown; p-values were calculated by Mann-Whitney test. (**G**) Representative H&E, Ki67, CD34, F4/80, and CD3 immunohistochemical micrographs of liver metastatic lesions found in NaCl- (red frame) and IFNα-treated (blue frame) mice, 21 days after intracecal injection of $CT26^{LM3}$ cells. Scale bar = 100 µm. (**H**) Quantification of the percentage of mice bearing liver metastases, as well as the percentage of tumor area and the number of cells expressing Ki67, CD34, F4/80, and CD3 per mm^2 determined by IHC. Immunohistochemical measurements were conducted on at least 1000 mm^2 of total liver area for both experimental conditions. Mean values ± SEM are shown; p-values were calculated by Mann-Whitney test.

The online version of this article includes the following source data and figure supplement(s) for figure 3:

Source data 1. Data for the graphs in the figure.

Figure supplement 1. In vivo selection of $CT26^{LM3}$ cells with increased spontaneous liver metastatic potential.

Figure supplement 1—source data 1. Data for the graphs in the figure.

Figure supplement 2. Immunophenotypic analysis of primary tumors and liver metastases in the orthotopic $CT26^{LM3}$ model.

Figure supplement 2—source data 1. Data for the graphs in the figure.

MRI analysis at day 21 after CRC challenge revealed that, in comparison with liver metastases observed in NaCl-treated controls, the lesions produced by MC38- or $MC38^{Ifnar1_KO}$ cells in IFNα-treated mice were similarly reduced in number and size (***Figure 4A and C–D***) and this resulted in comparable mouse survival rates (***Figure 4E***) in the absence of apparent myelotoxicity (***Figure 4—figure supplement 2A***). These data support the hypothesis that in our experimental setting the continuous IFNα administration has no direct antiproliferative activity towards CRC cells consistent with our previous reported data (***Figure 4—figure supplement 1A-C***; ***Catarinella et al., 2016***).

Next, we crossed *Ifnar1*-floxed mice (termed $Ifnar1^{fl/fl}$) (***Prigge et al., 2015***) with transgenic mice selectively expressing Cre recombinase in parenchymal and non-parenchymal liver cells (***Gerl et al., 2015***; ***Postic et al., 1999***; ***Wang et al., 2010***; ***Figure 4—figure supplement 1D***). Cell type-specific recombination was confirmed by crossing each parental mouse line with Rosa26-ZsGreen reporter mice. Note that by crossing the parental Cre-expressing lines with Rosa26-ZsGreen reporter mice (***Madisen et al., 2010***) the resultant mice showed specific recombination in most hepatocytes (identified by morphology), and liver fibroblast (GFP^+/$PDGFR\beta^+$), with about 98.2 ± 0.72% hepatic stellate cells that co-expressed GFP^+ and $PDGFR\beta^+$ signals (***Figure 4—figure supplement 1E, F***). Similarly, hepatic DCs (GFP^+/$CD11c^+$) had 94.17 ± 2.16% colocalization with GFP, while the colocalization percentage of $F4/80^+$ KCs or LCMs (GFP^+/$F4/80^+$) was 78.14 ± 5.03% (***Figure 4—figure supplement 1E,F***; ***Blériot and Ginhoux, 2019***; ***Karmaus and Chi, 2014***; ***Madisen et al., 2010***). Finally, HECs, including LSECs, (GFP^+/$CD31^+$) showed 85.3 ± 5.03% colocalization (***Figure 4—figure supplement 1E, F***), with no expression of GFP signals in cells other than $CD31^+$. $Ifnar1^{fl/fl}$ control mice and mice lacking *Ifnar1* in hepatocytes (termed Alb^{Ifnar1_KO}), hepatic stellate cells (termed $Pdgfrb^{Ifnar1_KO}$), $Itgax^+$ (CD11c) DCs/KCs/LCMs (termed $Itgax^{Ifnar1_KO}$) or $Cdh5^+$ + cells (termed $VeCad^{Ifnar1_KO}$) were intramesenterically injected with MC38 cells 7 days after NaCl or IFNα therapy initiation and did not show signs of hematotoxicity during IFNα infusion (***Figure 4—figure supplement 2B***). Metastatic growth was assessed by MRI at day 21 (***Figure 4B***). Loss of *Ifnar1* on hepatocytes, hepatic stellate cells or DCs/KCs/LCMs did not significantly alter the anti-metastatic activity of IFNα treatment (***Figure 4C, D and F*** and ***Figure 4—figure supplement 2C***). By contrast, the depletion of *Ifnar1* on HECs allowed the lesions to grow undisturbed (***Figure 4B***). Indeed, $VeCad^{Ifnar1_KO}$ mice treated with either NaCl or IFNα displayed very similar numbers and sizes of hepatic lesions (***Figure 4C and D***) or survival rates (***Figure 4F***), indicating that the antimetastatic properties of IFNα requires *Ifnar1* signaling on HECs. $VeCad^{Ifnar1_KO}$ mice exhibited increased tumor burden (***Figure 4D***) and mortality rates (***Figure 4—figure supplement 2D***) when compared to NaCl-treated $Ifnar1^{fl/fl}$ mice, suggesting that hepatic endothelial *Ifnar1* signaling exerts significant anti-tumor activity even in the context of physiologic endogenous intrahepatic levels of type I interferons. Furthermore, histological analysis of hepatic CRC lesions from

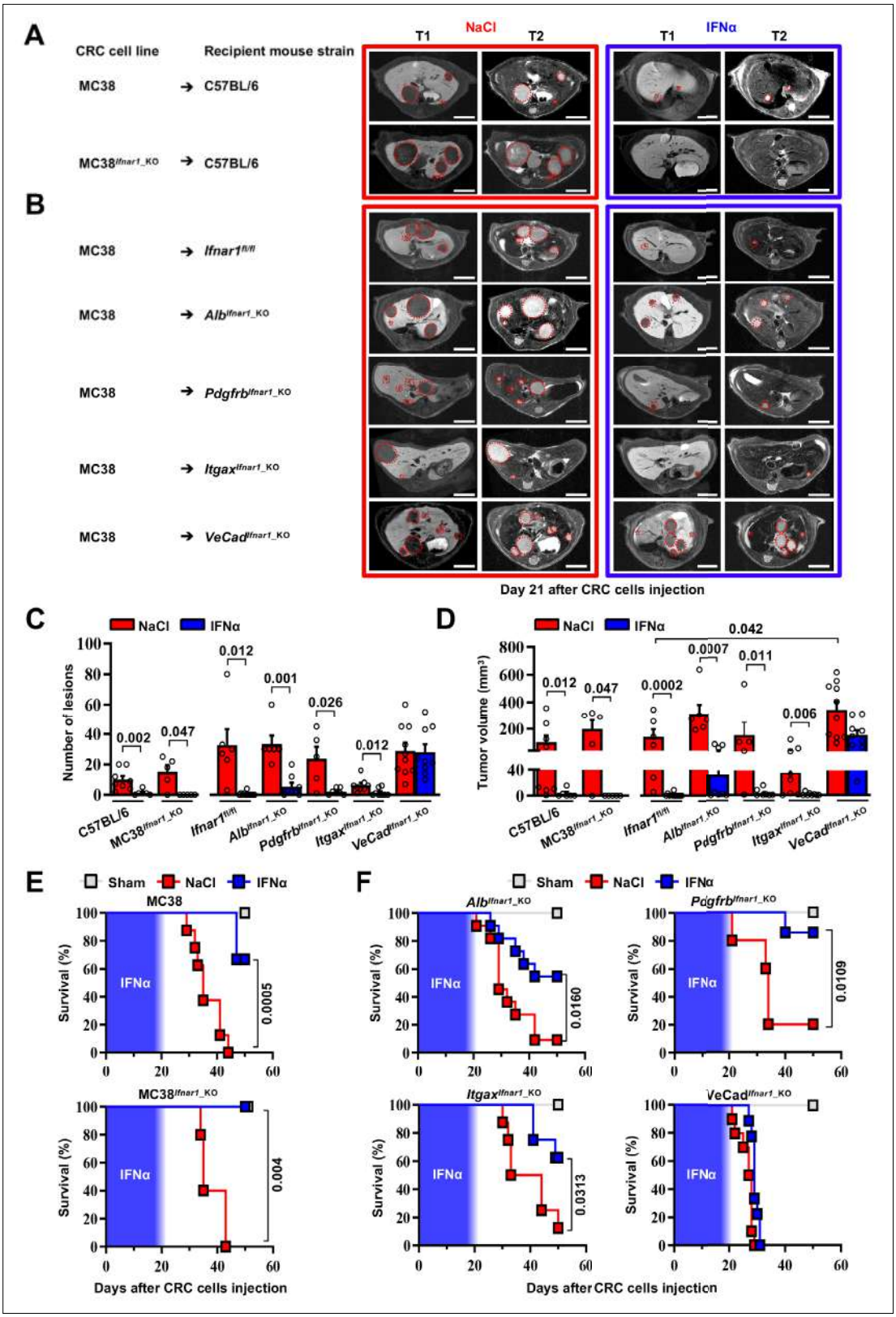

Figure 4. HECs mediate the antimetastatic activity of IFNα. (**A**) Representative hepatic contrast-enhanced MRI of wild-type mice (C57BL/6) at day 21 after injection of $5x10^4$ MC38 cells or $5x10^4$ MC38^{Ifnar1_KO} cells. Treatment with NaCl (red frame) and IFNα (blue frame) was initiated 7 days prior to intrasplenic injection of CRC cells. Red dashed lines highlight CRC liver metastases, characterized as hypointense and slightly-hyperintense regions in T1- and T2-weighted sequences, respectively. Scale bar = 5 mm. The number of mice for each experimental condition is also indicated.

Figure 4 continued on next page

Figure 4 continued

(**B**) Representative hepatic contrast-enhanced MRI at day 21 after MC38 intrasplenic injection of *Ifnar1*$^{fl/fl}$ mice and mice lacking *Ifnar1* on hepatocytes (*Alb*^{Ifnar1_KO}), hepatic stellate cells (*Pdgfrb*^{Ifnar1_KO}), CD11c-expressing DCs/KCs/LMCs (*Itgax*^{Ifnar1_KO}) and endothelial cells (*VeCad*^{Ifnar1_KO}) injected with 5x10^4 MC38 cells. Treatment with NaCl (red frame) and IFNα (blue frame) was initiated 7 days before MC38 cells intrasplenic injection. Red dashed lines highlight CRC liver metastases, characterized as hypointense and slightly-hyperintense regions in T1- and T2-weighted sequences, respectively. Scale bar = 5 mm. Number of mice for each experimental condition are also indicated. (**C**) Quantification of the number of hepatic lesions by MRI analysis, 21 days after CRC cells injection, of NaCl and IFNα-treated mice found in C57BL/6 mice, *Ifnar1*$^{fl/fl}$ mice and all conditional *Ifnar1*_KO mouse models described in (**A**) and (**B**). Mean values ± SEM are shown; p-values were calculated by Mann-Whitney test. (**D**) Quantification of total tumor volume of liver metastases by MRI analysis at day 21 after CRC intrasplenic injection of NaCl- and IFNα-treated mice found in C57BL/6 mice, *Ifnar1*$^{fl/fl}$ mice and all conditional *Ifnar1*_KO mouse models analyzed. Mean values ± SEM are shown; p-values were calculated by Mann-Whitney test. (**E**) Kaplan-Meier survival curves of C57BL/6 mice injected with MC38 cells (top) or MC38^{Ifnar1_KO} cells (bottom) described in (**A**). Sham injected animals (n=3) were used as control. The blue pattern indicates the time frame of IFNα ip release; p-values were calculated by log-rank/Mantel-Cox test. (**F**) Kaplan-Meier survival curves of the indicated groups of mice described in (**B**). Sham injected animals (n=3 per group) were used as control. The blue pattern indicates the time frame of IFNα ip release. The total number of mice for each experimental group were: NaCl-C57BL/6 n=8; IFNα-C57BL/6 n=6; NaCl-MC38^{Ifnar1_KO}-C57BL/6 n=5; IFNα-MC38^{Ifnar1_KO}-C57BL/6 n=6; NaCl-*Ifnar1*$^{fl/fl}$ n=6; IFNα-*Ifnar1*$^{fl/fl}$ n=11; NaCl-*Alb*^{Ifnar1_KO} n=6; IFNα-*Alb*^{Ifnar1_KO} n=8; NaCl-*Pdgfrb*^{Ifnar1_KO} n=5; IFNα-*Pdgfrb*^{Ifnar1_KO} n=7; NaCl-*Itgax*^{Ifnar1_KO} n=8; IFNα-*Itgax*^{Ifnar1_KO} n=8 and NaCl-*VeCad*^{Ifnar1_KO} n=10; IFNα-*VeCad*^{Ifnar1_KO} n=9. Data pooled from at least two independent experiments of each experimental group; p-values were calculated by log-rank/Mantel-Cox test.

The online version of this article includes the following source data and figure supplement(s) for figure 4:

Source data 1. Data for the graphs in the figure.

Figure supplement 1. Characterization of conditional *Ifnar1* knockout MC38 cells and liver specific *Ifnar1* knockout mouse models.

Figure supplement 1—source data 1. Original gel file and uncropped gel with labeling of panel (**A**).

Figure supplement 1—source data 2. Data for the graphs in the figure.

Figure supplement 1—source data 3. Original gel file and uncropped gel with labeling of panel (**D**).

Figure supplement 2. LSECs mediate the antimetastatic activity of IFNα.

Figure supplement 2—source data 1. Data for the graphs in the figure.

Figure supplement 3. Characterization of liver metastases developed in *VeCad*^{Ifnar1_KO} mice at day 21 after intramesenteric MC38 cells injection.

Figure supplement 3—source data 1. Data for the graphs in the figure.

NaCl- and IFNα-treated *VeCad*^{Ifnar1_KO} mice euthanized at day 21 after MC38 intramesenteric injection indicated that these tumors resembled NaCl-treated *Ifnar1*$^{fl/fl}$ lesions, showing signs of angiogenesis (as denoted by CD34 positivity) and similar content of F4/80$^+$ macrophages and CD3$^+$ T cells within the intrahepatic CRC foci (***Figure 4—figure supplement 3A, B***).

Continuous IFNα administration limits trans-sinusoidal migration of CRC cells by strengthening the liver vascular barrier

We next took advantage of fluorescence-based techniques to investigate the initial steps of liver colonization. First, we assessed the intrahepatic localization of GFP-expressing MC38 cells (MC38^{GFP}) (***Talamini et al., 2021***) that were intramesenterically challenged 5 min earlier. Most MC38^{GFP} cells in *Ifnar1*$^{fl/fl}$ or *VeCad*^{Ifnar1_KO} mice appeared physically trapped at the beginning of the sinusoidal circulation in both mouse lineages. This was evidenced by the close contact of MC38^{GFP} cells with LYVE-1-expressing LSECs in the proximity of the portal tracts (***Figure 5—figure supplement 1A***). Further, MC38^{GFP} cells arrested where the sinusoidal diameter (***Figure 5—figure supplement 1B***) is smaller than their own (12±0.1 μm), similar to what we previously reported (***Catarinella et al., 2016***). As the process of trans-sinusoidal migration – a critical limiting step in the metastatic cascade – is known to occur within 24 hr of CRC challenge (***Chambers et al., 2002***; ***Valastyan and Weinberg, 2011***; ***Wolf et al., 2012***), the intrahepatic number and localization of MC38^{GFP} cells were then studied at this time point. Confocal IF quantification revealed that, compared to NaCl-treated *Ifnar1*$^{fl/fl}$ animals, MC38^{GFP} cells were about ~twofold less abundant in IFNα-treated *Ifnar1*$^{fl/fl}$ mice and ~threefold more abundant in *VeCad*^{Ifnar1_KO} mice treated with NaCl or IFNα (***Figure 5A*** top). Moreover, confocal 3D reconstructions of liver sinusoids from IFNα-treated *Ifnar1*$^{fl/fl}$ mice unveiled that by 24 hr most MC38^{GFP} cells localize intravascularly (i.e. they did not invade the liver parenchyma), while in NaCl-treated *Ifnar1*$^{fl/fl}$ controls and in NaCl- or IFNα-treated *VeCad*^{Ifnar1_KO} mice only few MC38^{GFP} cells remain within the liver vasculature (i.e. they invaded the liver parenchyma) (***Figure 5A*** bottom, 5B and ***Figure 5—videos***

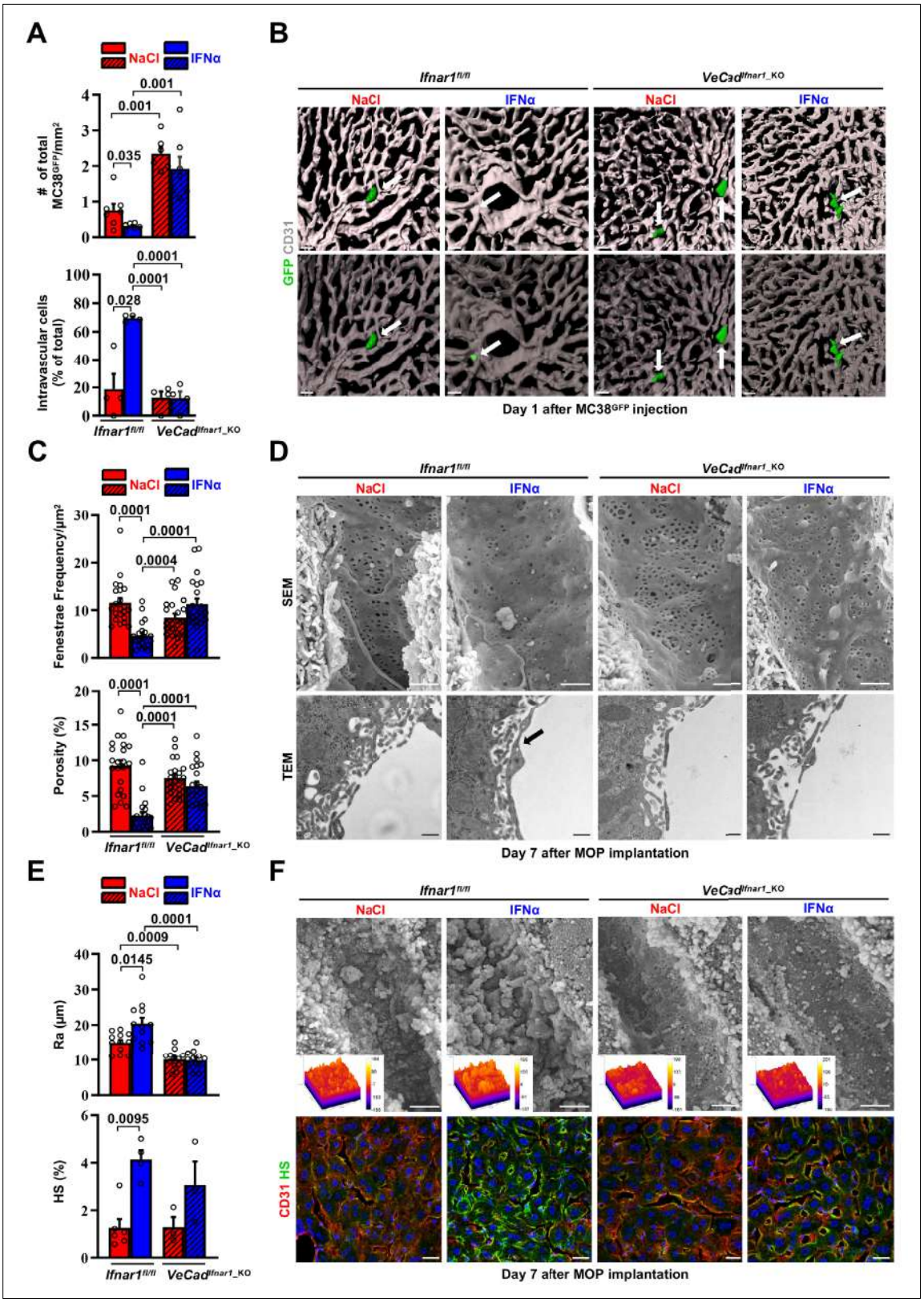

Figure 5. Continuous IFNα administration limits trans-sinusoidal migration of CRC cells by strengthening the hepatic vascular barrier. (**A**) Total number of MC38^{GFP} cells per area (top) and total number of intravascular MC38^{GFP} cells per tissue area (bottom). The total hepatic area was approximately 5 mm^2 for each experimental group. Intravascular localization was measured on 20 x images, 5 randomly selected images per mouse (n=3 per group). Mean values ± SEM are shown; p-values were calculated by Mann-Whitney test. (**B**) Confocal reconstruction of the liver vasculature from *Ifnar1*$^{fl/}$

Figure 5 continued on next page

Figure 5 continued

fl and *VeCad*^{Ifnar1_KO} mice 24 hr after MC38^{GFP} cells (green) intramesenteric vein injection in mice that were treated with NaCl or IFNα for 7 days. CD31 is shown in grey. To allow visualization of intravascular MC38^{GFP} cells and to enhance image clarity, the transparency of the sinusoidal rendering was increased up to 80% (bottom). Scale bars = 20μm. (**C**) Fenestrae frequency histogram (top) and percentage of vessel porosity (the percentage of liver endothelial surface area occupied by fenestrae, bottom) in liver sections of control *Ifnar1*$^{fl/fl}$ and *VeCad*$^{Ifnar1\text{-}KO}$ mice treated for 7 days with continuous NaCl or IFNα therapy. Quantification was performed on 17.000 x SEM images, 10 randomly selected images per mouse (n=3 per group). A total area of approximately 720 μm^2 of sinusoidal surface was analyzed for each mouse. Mean values ± SEM are shown; p-values were calculated by Mann-Whitney test. (**D**) Representative scanning electron micrographs (SEM, top) and transmission electron micrographs (TEM, bottom) images from liver sections of mice described in (**C**), showing hepatic fenestrations and endothelial features. Arrow indicates the increased endothelial thickness observed after continuous IFNα therapy in *Ifnar1*$^{fl/fl}$ mice. SEM scale bars = 1 μm; TEM scale bars = 500 nm. (**E**) Quantification of the arithmetical mean deviation or Ra coefficient (top) and the percentage of hepatic area positive for HS staining (bottom) on *Ifnar1*$^{fl/fl}$ and *VeCad*^{Ifnar1_KO} livers treated with continuous NaCl or IFNα therapy for 7 days. Quantification was performed on at least 3 *Ifnar1*$^{fl/fl}$ and *VeCad*^{Ifnar1_KO} livers per group. Mean values ± SEM are shown; p-values were calculated by Mann-Whitney test. (**F**) Liver sinusoidal endothelial glycocalyx (GCX) visualization by scanning electron micrographs (SEM, top) from *Ifnar1*$^{fl/fl}$ and *VeCad*^{Ifnar1_KO} livers that were perfused with lanthanum nitrate (a heavy metal that allows GCX visualization by stabilizing negatively charged GCX structures) 7 days after continuous NaCl or IFNα therapy. Scale bars = 1 μm. Inserts display a representation of the 3D topographic surface of a selected area within the liver sinusoid of each experimental condition. Representative immunofluorescence micrographs of Heparan sulfate (HS; green) and CD31 (red) staining from *Ifnar1*$^{fl/fl}$ and *VeCad*^{Ifnar1_KO} mice treated with continuous NaCl or IFNα therapy for 7 days, showing increased HS accumulation after IFNα therapy only in *Ifnar1*$^{fl/fl}$ mice (bottom). Hoechst (blue) was used for nuclear counterstaining. Scale bars = 20μm.

The online version of this article includes the following video, source data, and figure supplement(s) for figure 5:

Source data 1. Data for the graphs in the figure.

Source data 2. High-magnification immunofluorescence images of each channel.

Figure supplement 1. Continuous IFNα administration induces hepatic endothelial capillarization strengthening the liver vascular barrier.

Figure supplement 1—source data 1. Data for the graphs in the figure.

Figure supplement 1—source data 2. Collagen type IV.

Figure supplement 1—source data 3. Laminin.

Figure supplement 1—source data 4. ICAM1.

Figure supplement 1—source data 5. E-Selectin.

Figure supplement 2. Continuous IFNα administration induces hepatic endothelial capillarization that is reversed after discontinuation of IFNα therapy.

Figure supplement 2—source data 1. LYVE-1.

Figure supplement 2—source data 2. Data for the graphs in the figure.

Figure 5—video 1. 3D reconstruction of a representative extravasated MC38^{GFP} cell found within the liver parenchyma of a NaCl-treated *Ifnar1*$^{fl/fl}$ mouse.
https://elifesciences.org/articles/80690/figures#fig5video1

Figure 5—video 2. 3D reconstruction of an intravascular MC38^{GFP} cell found within a blood vessel of an IFNα-treated *Ifnar1*$^{fl/fl}$ mouse.
https://elifesciences.org/articles/80690/figures#fig5video2

Figure 5—video 3. 3D reconstruction of an extravasated MC38^{GFP} cell found within the liver parenchyma of a NaCl-treated *VeCad*^{Ifnar1_KO} mouse.
https://elifesciences.org/articles/80690/figures#fig5video3

Figure 5—video 4. 3D reconstruction of extravasated MC38^{GFP} cells found within the liver parenchyma of an IFNα-treated *VeCad*^{Ifnar1_KO} mouse.
https://elifesciences.org/articles/80690/figures#fig5video4

1–4). These results indicate that HECs, including LSECs, negatively control trans-sinusoidal CRC migration upon IFNα sensing.

To unravel phenotypic modifications associated with such antitumor function of HECs, including LSECs, the liver microvasculature of NaCl- or IFNα-treated *Ifnar1*$^{fl/fl}$ and *VeCad*^{Ifnar1_KO} mice was analyzed by scanning electron microscopy (SEM) and transmission electron microscopy (TEM). IFNα treatment of *Ifnar1*$^{fl/fl}$ mice significantly decreased the frequency of sinusoidal fenestrae and the overall porosity of LSECs (***Figure 5C and D*** top), while it increased: (i) the endothelial thickness (***Figure 5—figure supplement 1D***), (ii) the space of Disse density (an indirect measure of hepatocyte microvilli density) (***Figure 5—figure supplement 1D***; ***Gissen and Arias, 2015***), (iii) the subendothelial deposition of collagen fibrils (***Figure 5—figure supplement 1D***) and (iv) the appearance of a basal lamina (***Figure 5D*** bottom and ***Figure 5—figure supplement 1D***). These results were corroborated by immunofluorescence analysis assessing an enhanced perivascular expression of Collagen type IV and Laminin (***Figure 5—figure supplement 1E, F***), two components of the basal lamina previously shown to form a barrier against tumor cell invasion (***Mak and Mei, 2017***; ***Tanjore and Kalluri, 2006***).

By contrast, IFNα treatment of *VeCad*^{Ifnar1_KO} mice failed to significantly support these changes, leaving the liver microvasculature of these animals highly similar to that of liver metastases-permissive NaCl-treated *Ifnar1*$^{fl/fl}$ controls (***Figure 5C and D*** and ***Figure 5—figure supplement 1D-F***). Moreover, IFNα treatment of *Ifnar1*$^{fl/fl}$ mice significantly increased the expression of LYVE-1, a marker of hepatic capillarization (***Pandey et al., 2020***; ***Wohlfeil et al., 2019***). By contrast, IFNα treatment of *VeCad*^{Ifnar1_KO} mice showed no effect (***Figure 5—figure supplement 2A,B***).

Next, we evaluated the status of the vascular glycocalyx (GCX), a fibrous network of glycoproteins and proteoglycans that lines the LSECs and projects intraluminally (***Reitsma et al., 2007***). Notably, enhanced GCX deposits can act as a repulsive barrier that prevents tumor cell interactions with endothelial cells, adhesion molecules or chemokines have been previously identified as negative correlates of transendothelial migration (***Glinskii et al., 2005***; ***Mitchell and King, 2014***; ***Offeddu et al., 2021***; ***Wilkinson et al., 2020***). Continuous IFNα treatment modified this network as well, increasing its thickness (***Figure 5E and F*** top) and the expression of one of its major components, the heparan sulfate (HS) (***Reitsma et al., 2007***; ***Figure 5E and F*** bottom). Of note, *VeCad*^{Ifnar1_KO} mice displayed reduced GCX thickness independently of NaCl- or IFNα-treatment (***Figure 5E and F***). Additionally, we evaluated the vascular and perivascular status of cell adhesion molecules such as selectins and integrins, which have been positively associated with the transendothelial migration of tumor cells (***Glinskii et al., 2005***; ***Wilkinson et al., 2020***). The expression of ICAM1, E-Selectin (CD62E) (***Figure 5—figure supplement 1G,H***) and the integrins ITGB2 (CD18) or ITGA4 (CD49d) (***Figure 5—figure supplement 1C***) was up-regulated in IFNα-treated *Ifnar1*$^{fl/fl}$ controls, while significantly reduced or attenuated in IFNα-treated *VeCad*^{Ifnar1_KO} mice. The notion that a more modest upregulation of some these markers was still evident in the latter mice may reflect the capacity of liver cells other than HECs to respond to IFNα. Altogether, these results indicate that numerous phenotypic modifications of the liver microvasculature previously associated with the deficient extravasation of both normal and transformed cells of different origin (***Guidotti et al., 2015***; ***Valastyan and Weinberg, 2011***) also occur because of continuous IFNα sensing by HECs, including LSECs. Notably, these microvascular modifications were reverted after the discontinuation of IFNα therapy with no impact on long-term liver functionality/viability (***Figure 5—figure supplement 2C-I***).

HECs acquire an antimetastatic transcriptional profile upon continuous IFNα sensing

To confirm the above-mentioned data and to shed new light on the transcriptional changes that HECs adopt to limit CRC trans-sinusoidal migration, we performed RNA-seq analyses on CD31^{+} endothelial cells isolated from the liver of *Ifnar1*$^{fl/fl}$ or *VeCad*^{Ifnar1_KO} mice 7 days after NaCl or IFNα treatment (***Figure 6—figure supplement 1A***). Using SEM to assess the % of CD31^{+} cells bearing the typical sinusoidal fenestrae, we determined that our preparations contain ~96% of bona-fide LSECs (***Figure 6—figure supplement 1B***), consistently to previous reports (***Liu et al., 2011***; ***Su et al., 2021***). When compared to HECs isolated from NaCl-treated *Ifnar1*$^{fl/fl}$ mice, HECs derived from IFNα-treated animals of the same lineage showed 381 transcripts that were differentially expressed (***Figure 6A***). As expected, many of these up-regulated transcripts belonged to the ISG family, including *Irf7, Irf9, Mx1, Mx2, Isg15, Stat1,* and *Oasl1* (***Figure 6A and B***). Pre-ranked gene set enrichment analyses (GSEA) of IFNα-treated LSECs also revealed a significant enrichment of transcripts involved in interferon signaling or in the induction of varying cytokines and chemokines (***Figure 6C***). Several transcripts related to the ECM/GCX organization or the cell-cell/cell-matrix adhesion pathways were upregulated as well (***Figure 6B and D***). Of note, the expression of *Itga4* and *Itgb2* – previously shown to be increased by IFNα treatment at the protein level (***Figure 5—figure supplement 1C***) – was also enhanced at the transcriptional level (***Figure 6B***). A similar association did not hold true for *Icam1* and *Sele*, suggesting that the increased protein expression we observed earlier (***Figure 5—figure supplement 1G***) occurred independently of transcriptional activity (***Figure 6B***). Notably, GSEA also identified gene sets involved in the IFNα-dependent activation of innate and adaptive immune responses or in TCR-dependent signaling pathways (***Figure 6—figure supplement 1C***).

Keeping the HECs transcriptional profile of NaCl-treated *Ifnar1*$^{fl/fl}$ mice as a point of reference, a total of 566 genes were differentially expressed (DEGs) in HECs isolated from NaCl-treated *VeCad*^{Ifnar1_KO} mice, of which 373 (mostly ISGs and genes involved in the immune response or in the antigen processing) were downregulated (***Figure 6A–C***). These latter results indirectly suggest that – when

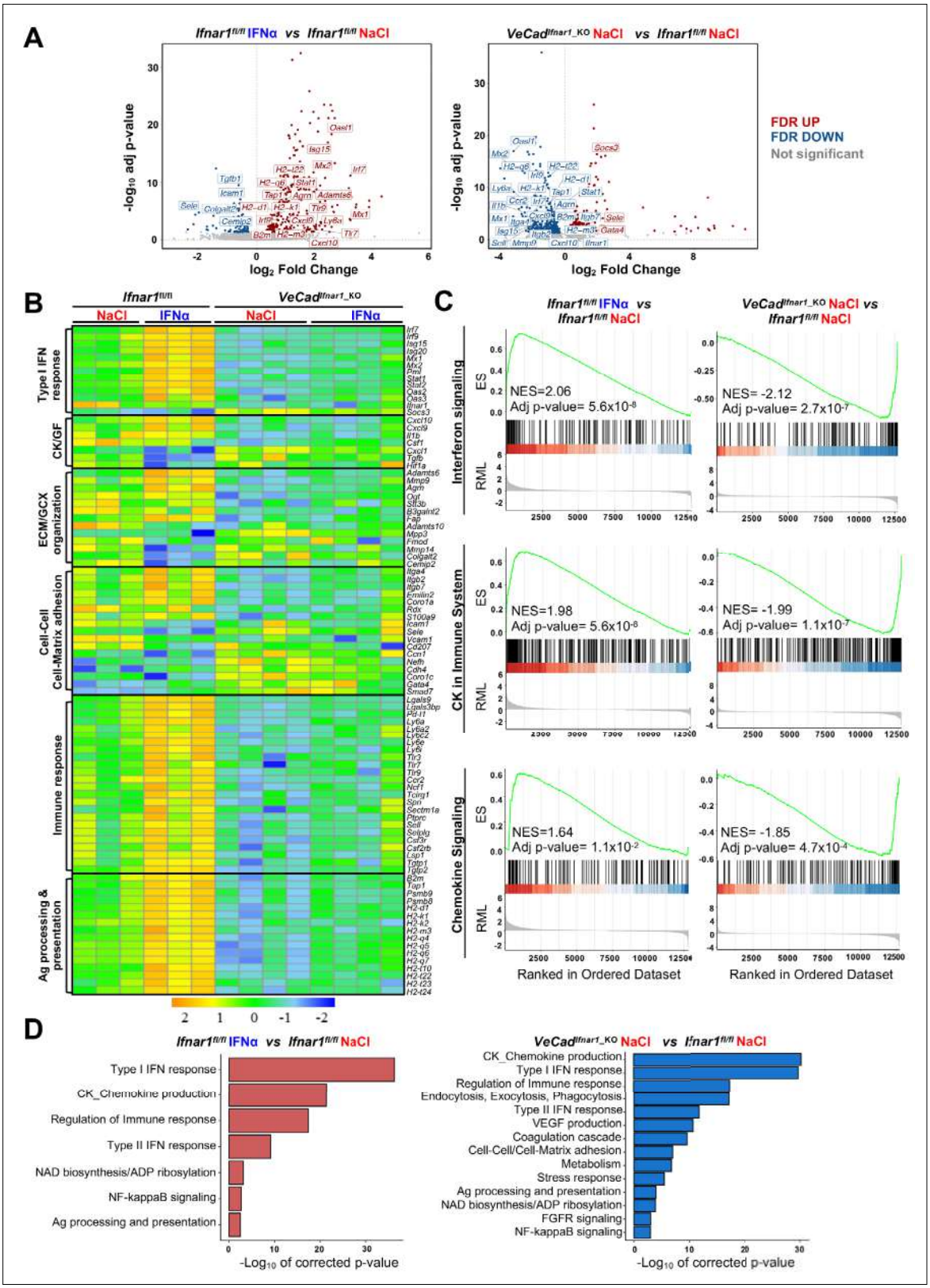

Figure 6. HECs acquire an antimetastatic transcriptional profile upon continuous IFNα sensing. (**A**) Volcano plots of differential gene expression (DGE) results obtained from the comparisons between HECs-derived from *Ifnar1*$^{fl/fl}$ mice treated with NaCl and IFNα for 7 days (left) and between HECs-derived from *VeCad*^{Ifnar1_KO} and *Ifnar1*$^{fl/fl}$ NaCl-treated mice (right) (*Ifnar1*$^{fl/fl}$ n=3; *VeCad*^{Ifnar1_KO} n=4). Significant false discovery rate (FDR <0.05) up- and down-regulated genes are highlighted in red and blue colors, respectively, not significant genes are depicted in grey. (**B**) Heatmap of the expression

Figure 6 continued on next page

Figure 6 continued

values (log2-transformed rpkm) of manually selected genes retrieved from differentially regulated pathways. (**C**) Pre-ranked Gene Set Enrichment Analysis (GSEA) enrichment plots of the indicated pathways between CD31$^+$ cells from *Ifnar1*$^{fl/fl}$-IFNα and *Ifnar1*$^{fl/fl}$-NaCl (left) and between *VeCad*^{Ifnar1_KO}-NaCl and *Ifnar1*$^{fl/fl}$-NaCl-treated animals (right). (**D**) Bar charts showing the adjusted p-values (-log10 transformed) of selected pathways from the enrichment analysis performed on comparisons between *Ifnar1*$^{fl/fl}$-IFNα and *Ifnar1*$^{fl/fl}$-NaCl CD31$^+$ cells (left graph) and between *VeCad*^{Ifnar1_KO}-NaCl and *Ifnar1*$^{fl/fl}$-NaCl CD31$^+$ cells (right graph).

The online version of this article includes the following source data and figure supplement(s) for figure 6:

Source data 1. Gene Ontology (GO) of biological process enrichment analysis of all differentially expressed genes.

Figure supplement 1. HECs acquire an antimetastatic transcriptional profile upon continuous IFNα sensing.

Figure supplement 1—source data 1. Data for the graphs in the figure.

compared to HECs capable of sensing low levels of endogenous type I IFNs, as those present in NaCl-treated *Ifnar1*$^{fl/fl}$ mice – LSECs devoted of *Ifnar1* may be less prepared to stimulate innate and adaptive immunity (***Figure 6B***). The downregulation of transcripts involved in cell-cell adhesion molecules and matrix remodeling (***Figure 6—figure supplement 1D***) further suggests a relative unpreparedness of *VeCad*^{Ifnar1_KO} HECs at accommodating changes that may confer protection against CRC trans-sinusoidal cell migration. Along these lines, the upregulation of the transcripts for *Gata4* -a master-regulator of liver sinusoidal differentiation which leads to liver fibrosis deposition upon its loss (***Winkler et al., 2021***)- and *Smad7* – an inhibitor of transforming growth factor-beta (TGF-β)-dependent subendothelial matrix deposition causative of sinusoidal capillarization (***Tauriello et al., 2018***) – in HECs isolated from NaCl-treated *VeCad*^{Ifnar1_KO} mice (***Figure 6A***) could be interpreted as a diminished capacity to shape a vascular antimetastatic barrier. Finally, Gene Ontology (GO) analysis of HECs confirmed that *Ifnar1*-proficient, but not *Ifnar1*-deficient, HECs upregulate transcriptional pathways involved in the production of immunostimulatory cytokines and chemokines, the capacity to process and present antigens or the regulation of immune responses (***Figure 6D***). Altogether, the data support the hypothesis that, upon IFNα sensing, HECs and particularly LSECs not only acquire a transcriptional profile that can reinforce their barrier function, but they may also enhance HECs/LSECs immunostimulatory functions contributing to antitumor activity.

Continuous IFNα sensing improves immunostimulatory properties of HECs to provide long-term tumor protection

First, HECs/LSECs isolated from the liver of *Ifnar1*$^{fl/fl}$ or *VeCad*^{Ifnar1_KO} mice 7 days after continuous NaCl or IFNα treatment were assessed for the relative surface protein expression of MHC-I, CD86 (a costimulatory molecule ***Katz et al., 2004***) or the interleukin 6 receptor alpha (IL-6RA, a molecule that LSECs use to properly cross-prime antigens to naïve CD8$^+$ T cells ***Böttcher et al., 2014***). Following IFNα treatment, *Ifnar1*-bearing LSECs significantly increased MHC-I, CD86 and IL-6RA expression (***Figure 7—figure supplement 1A***), while no induction was detected in *Ifnar1*-negative LSECs (***Figure 7—figure supplement 1A***). We then analyzed the ability of IFNα-treated LSECs or splenic DCs (sDCs) from *Ifnar1*$^{fl/fl}$ and *VeCad*^{Ifnar1_KO} mice to stimulate the cross-priming of naive CD8$^+$ T cells in vitro. To this end, viable CD31$^+$ HECs and CD11c$^+$ sDCs were isolated and purified (***Figure 7—figure supplement 2A***, B). sDCs were cultured to acquire mature CD8α$^+$ (~25%) or plasmacytoid (45%–50%) phenotypes endowed with cross-priming capacity (***Figure 7—figure supplement 2C, D***; ***Fu et al., 2020***). HECs and sDCs from *Ifnar1*$^{fl/fl}$ or *VeCad*^{Ifnar1_KO} mice previously pulsed with the SIINFEKL peptide or soluble ovalbumin (sOVA) in the presence or absence of either IFNα or NaCl were then co-cultured with naive OT-I CD8$^+$ T cells and their relative cross-priming capacity was defined by the percentage of these latter cells to express both CD44 and IFNγ (***Figure 7—figure supplement 1B***). IFNα stimulation of *Ifnar1*-bearing HECs (HECs from *Ifnar1*$^{fl/fl}$ mice or sDCs from *Ifnar1*$^{fl/fl}$ and *VeCad*^{Ifnar1_KO} mice) pulsed with SIINFEKL or sOVA promptly increased their cross-priming capacities, while the same IFNα treatment failed to do so in *Ifnar1*-negative cells (HECs from *VeCad*^{Ifnar1_KO} mice) (***Figure 7A and B*** and ***Figure 7—figure supplement 1B, C***). Once exposed to IFNα and pulsed with sOVA, HECs and sDCs from *Ifnar1*$^{fl/fl}$ mice cross-primed naïve OT-I CD8$^+$T cells to a similar extent (***Figure 7B*** and ***Figure 7—figure supplement 1C***), highlighting once more the immunostimulating potential of IFNα treatment on HECs, including LSECs. We also evaluated the splenic composition of central memory T cell populations (Tcm, CD8$^+$CD44$^+$CD62L$^+$) (***Figure 7C*** and ***Figure 7—figure***

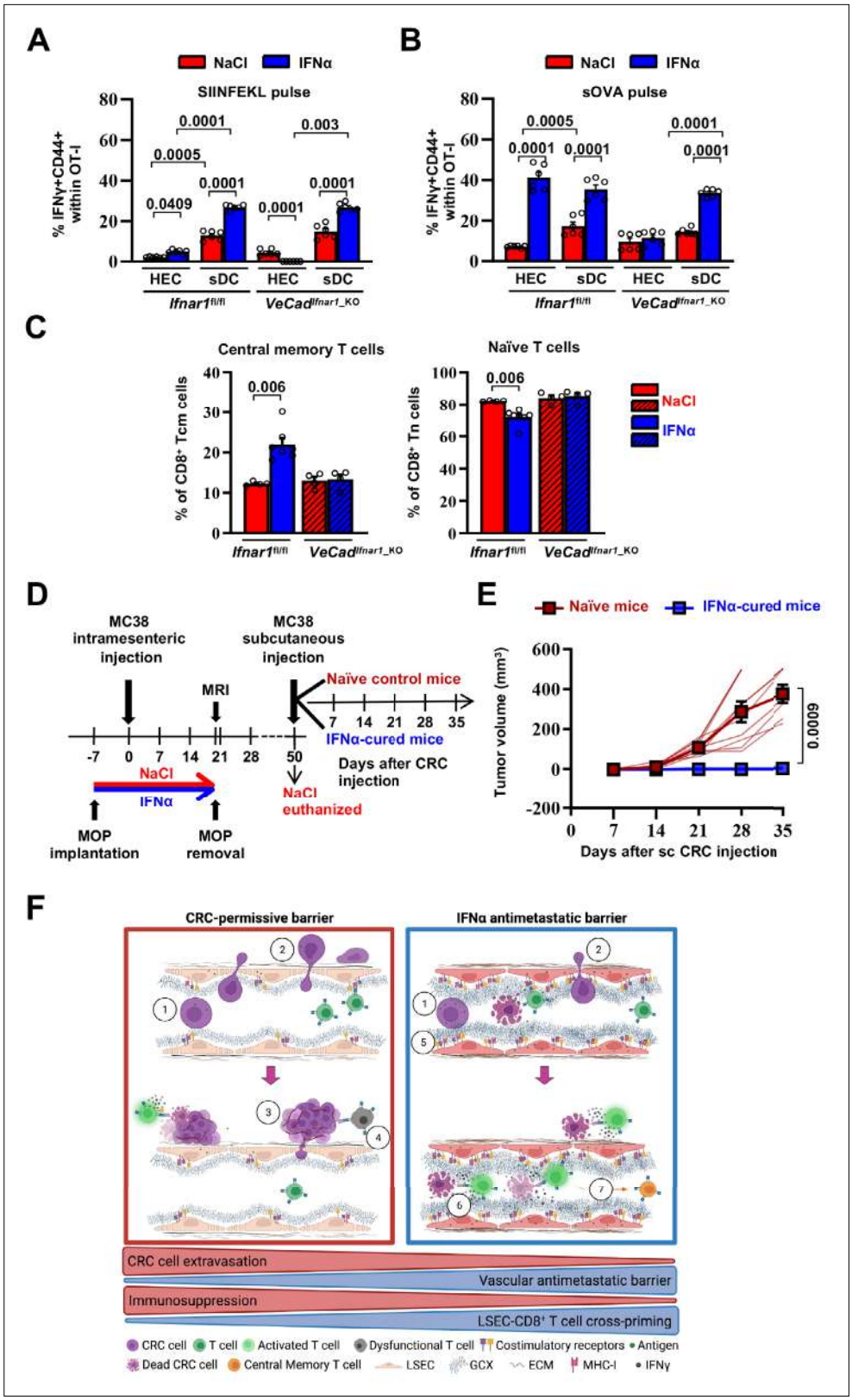

Figure 7. Continuous IFNα sensing improves immunostimulatory properties of HECs to provide long-term tumor protection. (**A–B**) Quantification of the percentage of OT-I CD8$^+$ T cells expressing CD44$^+$IFNγ$^+$ generated after the co-cultured with HECs, including LSECs, or sDCs isolated from *Ifnar1*$^{fl/fl}$ and *VeCad*$^{Ifnar1\text{-}KO}$ mice and stimulated with SIINFEKL peptide (**A**) or soluble OVA protein (sOVA) (**B**) in the presence of NaCl or IFNα. Mean values ± SEM are

Figure 7 continued on next page

Figure 7 continued

shown; p-values were calculated by two-way ANOVA test from two independent experiments with three biological replicates each. (**C**) Quantification of the percentage of splenic T central memory (Tcm, $CD8^+CD44^+CD62L^+$) and naïve T cells (Tn, $CD8^+CD44^-CD62L^+$) populations 21 days after intramesenteric MC38 cells injection into NaCl- or IFNα-treated *Ifnar1*$^{fl/fl}$ and *VeCad*^{Ifnar1_KO} mice. Quantification was performed on least 4 mice per group. Mean values ± SEM are shown; p-values were calculated by Mann-Whitney test. (**D**) Schematic representation of the experimental procedure used for tumor rechallenge. IFNα-*Ifnar1*$^{fl/fl}$-cured mice and naïve *Ifnar1*$^{fl/fl}$ mice were subcutaneously rechallenged with $5x10^3$ MC38 cells and received no further treatment. Tumor growth was monitored weekly for 35 days. Note that we used aged-matched *Ifnar1*$^{fl/fl}$ naïve mice because NaCl-treated mice had to be euthanized for ethical reasons by day 50. (**E**) Kinetics of subcutaneous tumor growth in naïve (n=10) and IFNα-cured (n=7) mice. Both, mean tumor volume and individual animal measurements are shown. Mean values ± SEM are shown; p-values were calculated by two-way ANOVA test. (**F**) Schematic model: CRC cells emerging from the primary tumor reach the hepatic sinusoids via the portal circulation and arrest - mostly because of size constrains - at the portal side of the sinusoidal circulation (1), CRC cells trans-sinusoidally migrate into the liver parenchyma (2) and develop micro-metastases that will eventually grow overtime (3; red frame), promoting the generation of an immunosuppressive microenvironment leading to dysfunctional T cells (4; red frame). Conversely, IFNα therapy (blue frame), by modifying LSECs porosity, thickness, deposition of basal membrane and GCX depth, builds up a vascular antimetastatic barrier (5), that impairs CRC trans-sinusoidal migration, promoting intravascular containment of invading tumor cells (6) that together with IFNα-mediated increased cross-presentation and cross-priming by HECs/LSEC, will lead to naïve $CD8^+$ T cell activation and secondary generation of long-term antitumor immunity and protection from secondary tumor challenge (7). Created with https://biorender.com/.

The online version of this article includes the following source data and figure supplement(s) for figure 7:

Source data 1. Data for the graphs in the figure.

Figure supplement 1. Continuous IFNα sensing improves immunostimulatory properties of HECs to provide long-term tumor protection.

Figure supplement 1—source data 1. Data for the graphs in the figure.

Figure supplement 2. Isolation and flow cytometry characterization of HECs and sDCs.

supplement 1D) as a proxy of potential systemic memory responses against tumor antigens (***Sallusto et al., 2004***; ***Stone et al., 2009***; ***Yu et al., 2019***). Splenic naive T cells (Tn, $CD8^+CD44^-CD62L^+$) were also evaluated. Looking at *Ifnar1*$^{fl/fl}$ or *VeCad*^{Ifnar1_KO} mice continuously treated with NaCl or IFNα and euthanized by day 21 after challenge, we found that only IFNα-treated *Ifnar1*$^{fl/fl}$ mice showed an increased proportion of Tcm and decreased percentage of Tn when compared to NaCl-treated *Ifnar1*$^{fl/fl}$ controls (***Figure 7C***), suggesting that IFNα-responsive LSECs may promote antitumor immune memory in secondary lymphoid organs.

To assess whether IFNα-stimulated HECs and LSECs promoted memory responses endowed with antitumor potential, *Ifnar1*$^{fl/fl}$-cured mice (defined as animals that 7 days after IFNα treatment initiation were intramesenterically challenged with MC38 cells and survived as disease-free animals until day 50) or naive *Ifnar1*$^{fl/fl}$ control mice were subcutaneously rechallenged with MC38 cells (***Figure 7D***). Notably, while the latter animals developed subcutaneous tumors that increased in size over time, none of the *Ifnar1*$^{fl/fl}$-cured mice showed detectable lesions at any time point studied (***Figure 7E***). These results indicate that continuous IFNα treatment promotes protection against secondary tumor challenge even after IFNα therapy discontinuation. The results also suggest that this effect may be dependent on the capacity of IFN-sensitive HECs and LSECs to foster antitumor immunity, especially tumor-specific effector $CD8^+$ T cell responses that are well-known to control tumor growth in vivo in different experimental settings (***Dobrzanski et al., 2000***; ***Katlinski et al., 2017***; ***Klebanoff et al., 2005***; ***Yu et al., 2019***).

Discussion

In this study, we used different mouse models of CRC liver metastasis to show that the continuous perioperative administration of relatively low IFNα doses provides significant antitumor potential in vivo without provoking overt toxicity. Moreover, under the pharmacological conditions we defined (route, dosage, treatment duration, and chemical nature of the recombinant protein), we did not observe counter-regulatory mechanisms affecting IFNα efficacy (***Katlinski et al., 2017***), or significant systemic side effects, as our strategy avoids the short tissue-oscillatory IFNα bursts that are

often achieved after high and pulsed administrations, often associated with efficacy-limiting toxicities (**Weber et al., 2015**). These results are consistent with previous preclinical work indicating that the intrahepatic delivery of IFNα through a gene/cell therapy approach curbs CRC liver metastases by acting primarily on unidentified non-hematopoietic stromal cell populations (**Catarinella et al., 2016**).

Given the pleotropic nature of IFNα, we demonstrated that the antimetastatic activity of IFNα is neither based on the direct inhibition of primary intracecal tumor growth, favoring the hypothesis that IFNα therapy does not modify the number of cells that spread from primary tumors and seed into the liver – nor on the direct inhibition of metastatic cell growth within the liver. These data are consistent with the high IFNα concentrations required to activate the 'tunable' direct antiproliferative functions of this cytokine, likely exceeding the levels achieved in our system (**Catarinella et al., 2016**; **Schreiber, 2017**). In addition, IFNα therapy does not require indirect stimulation of hepatocytes, HSCs, DCs, KCs, or LCMs to exert its antimetastatic functions. Rather, the results pinpointed HECs/LSECs as key local and early sensors of IFNα that ultimately limit CRC cell invasion into the liver.

Mechanistically, we showed that IFNα-stimulated LSECs inhibit the trans-sinusoidal migration of circulating CRC cells normally occurring within 24 hr of their initial intrahepatic landing. This effect is associated with phenotypic changes that IFNα-stimulated LSECs acquire or induce in the liver microenvironment. Among these changes, we observed a reduction in the overall LSEC porosity (i.e. sinusoidal fenestrae were reduced in number and size), an enhancement in the subendothelial deposition of basal membrane components (including Collagen IV and Laminin) and an upregulation of LYVE-1, a marker of hepatic capillarization (**Pandey et al., 2020**; **Wohlfeil et al., 2019**). Along these lines, it is noteworthy that in the 'healthy' liver, functioning as a common site for CRC metastases, LSECs contain numerous fenestrae of up to 200 nm in diameter and normally lack the typical basal membrane that characterizes the microvasculature of most other tissues and organs (**Jacobs et al., 2010**). It is also interesting to note that IFNα-stimulated LSECs promote microvascular alterations like those typifying pathological conditions (e.g. initial hepatic capillarization and liver fibrosis **Pandey et al., 2020**; **Wohlfeil et al., 2019**) associated with impaired immune cell extravasation and reduced immune surveillance (**Guidotti et al., 2015**) and reduction of hepatic metastases from solid tumors including CRCs (**Wohlfeil et al., 2019**). This fits with the evidence that CRC patients suffering from chronic viral liver fibrotic diseases characterized by hepatic endogenous type I interferon production display lower incidence of hepatic metastases (**Augustin et al., 2013**; **Baiocchini et al., 2019**; **Li Destri et al., 2013**). The existence that fibrotic liver diseases not associated with reduced metastatic risk (**Kondo et al., 2016**) suggests that changes in the vascular hepatic niche other than matrix deposition play additional roles in this process. Indeed, IFNα stimulated LSEC-governed changes hampering CRC extravasation including the modification of the sinusoidal GCX that, by increasing its thickness and modifying its chemical composition, recapitulated conditions known to negatively regulate the trans-endothelial migration of tumor cells in other settings (**Glinskii et al., 2005**; **Mitchell and King, 2014**; **Offeddu et al., 2021**; **Wilkinson et al., 2020**). The continuous administration of therapeutic low-doses of IFNα thus stimulate HECs/LSECs to shape a vascular antimetastatic barrier preventing the interaction between tumor cells and endothelial cells that are known to promote the extravasation of the former cells (**Glinskii et al., 2005**; **Mitchell and King, 2014**; **Wilkinson et al., 2020**). Accordingly, the enhanced expression of 'pro-migratory' adhesion molecules and integrins that we observed in the liver of animals bearing IFNα-responsive LSECs appear to be efficiently counteracted by the creation of such vascular barrier.

Of note, the functional consequences of LSEC capillarization (especially the induction of hepatic fibrosis) during states of chronic liver injury highly depend on the relative magnitude and duration of the underlying liver disease (**DeLeve, 2015**). Additionally, both LSEC capillarization and hepatic fibrosis are reversed when chronic liver injury resolves (**DeLeve, 2015**). In keeping with these concepts and the absence of sALT elevation or morphological evidence of liver disease during continuous IFNα therapy, it is not surprising that we observed a complete recovery of fenestrae abundance and LSEC porosity 40 days after therapy discontinuation. This supports the notion that a continuous but relatively short IFNα therapy promotes changes in the structure and function of LSECs that are mild and reversible and should not result in persistent hepatic fibrinogenesis. Such notion is also supported by the absence of hepatic toxicity (**Weber et al., 2015**) and the significant reduction in established fibrosis in patients with chronic viral liver diseases treated with recombinant IFNα for up to 48 weeks (**Li et al., 2019**; **Poynard et al., 2002**). The notion that IFNα treatment failed to shape the vascular

antimetastatic barrier in mice carrying the *Ifnar1*-deficiency only in endothelial cells further strengthens this hypothesis and places HECs/LSECs at a center of a relevant antitumor process ultimately limiting CRC liver invasion. This concept is also indirectly supported by the fact that the increased expression *Gata4* -a master-regulator of liver sinusoidal differentiation which leads to liver fibrosis deposition upon its loss (**Winkler et al., 2021**) - and *Smad7* – an inhibitor of transforming growth factor-beta (TGF-β) dependent subendothelial matrix deposition and sinusoidal capillarization (**Tauriello et al., 2018**) were not downregulated by IFNα treatment in mice in which all cell types except LSECs could sense this cytokine, thus loosening the hepatic vascular barrier.

In addition, to hindering the initial trans-sinusoidal migration of CRC cells in vivo, IFNα-stimulated LSECs efficiently cross-presented nominal tumor antigens to naive $CD8^+$ T cells in vitro, enabling degrees of T cell priming and effector differentiation that were comparable to those induced by professional APCs. In keeping with this, we demonstrated that the in vivo IFNα stimulation of LSECs resulted in the upregulation of proteins and transcripts associated with antigen processing and presentation or co-stimulation (e.g. MHC-I, CD86, IL-6RA, *B2m, Tap1, Psmb-8/9 and H2-d1, H2-k1/2*) (**Böttcher et al., 2014**; **Katz et al., 2004**; **Montoya et al., 2002**; **Rodriguez et al., 1999**). Moreover, our results also suggest that IFNα-stimulated LSECs may play a key role in antitumor immunity, as mice were protected from secondary tumor rechallenge even after discontinuation of IFNα treatment. The fact that the same IFNα therapy also significantly increased the overall number of central memory T cells in the spleen while decreasing that of naive T cells (**Sallusto et al., 2004**; **Yu et al., 2019**) further suggests a role for IFNα-stimulated LSECs in the generation of systemic and protective long-term antitumor immunity.

These data are consistent with the notion that IFNα-stimulated LSECs, due to their anatomical proximity and efficient endocytosis capacity that is among the highest of all cell types in the body (**Sorensen and Smedsrod, 2020**) – rapidly remove CRC-derived antigens from the intravascular space and productively and rapidly contribute to the development of effective antitumor immunity, since this process does not require the time-consuming step of migration to lymphatic tissue (**Böttcher et al., 2014**). This concept is also supported by the upregulation by IFNα-stimulated LSECs of *Cxcl9* and *Cxcl10*, two chemokines involved in the attraction and retention of naïve T cell populations of lymphocytes into the liver (**Franciszkiewicz et al., 2012**), a necessary step for the generation of an efficient antitumor immune response. Additionally, other cell types within the hepatic niche could further amplify this IFNα-initiated cascade, as it has been shown that dendritic cells releasing IFNα also reduce liver metastatic colonization by CRC cells (**Toyoshima et al., 2019**) and that this cytokine properly polarizes the tumor microenvironment (**Catarinella et al., 2016**; **De Palma et al., 2008**). On the contrary, the notion that a minority of IFNα-treated animals develop small intrahepatic lesions that display similar proliferation, neoangiogenic and immunologic markers than untreated lesions highlights the possibility that CRC tumors, once established as macroscopic metastases, may become refractory and resistant to IFNα therapy by downregulating *Ifnar1* (**Boukhaled et al., 2021**; **Katlinski et al., 2017**). This would be consistent with the lack of efficacy of our approach in established orthotopic tumors within the cecal wall.

Altogether, we have identified a novel MoA by which IFNα functions as antitumor drug against CRC liver metastases. Whether the adoption of similar LSEC-stimulating IFNα treatments may also curb the hepatic growth of metastatic cells originating from other solid tumors, or if continuous IFNα treatment promote the generation of vascular barriers in other metastasis-prone organs remains to be determined (**Crist and Ghajar, 2021**). Based on the findings of this report, we propose the following model: CRC cells emerging from the primary tumor reach the hepatic sinusoids via the portal circulation and arrest – mostly because of size constrains – at the portal side of the sinusoidal circulation. CRC cells then trans-sinusoidally migrate into the liver parenchyma and develop micrometastases that will eventually grow overtime, promoting the generation of an immunosuppressive microenvironment. Continuous therapy with well-tolerated doses of recombinant IFNα, stimulates HECs/LSECs to limit CRC trans-sinusoidal migration and parenchymal invasion by building up a vascular barrier typified by the reduction of LSECs porosity, the increased thickness of GCX and the appearance of a basal membrane. Continuous IFNα therapy also promotes long-term antitumor immunity in cured mice and protection from secondary tumor challenge, by stimulating LSECs to efficiently cross-prime tumor antigens to naïve $CD8^+$ T cells (**Figure 7F**).

In terms of future clinical applications, our strategy could be used as perioperative neoadjuvant immunotherapy in CRC patients undergoing resection of their primary tumor who are at high risk for developing metachronous liver metastases (**Engstrand et al., 2019**; **van Gestel et al., 2014**). Indeed, several technologies have already been developed for the sustained release of drugs, such as osmotic pumps, electronic devices, hyaluronic acid-based hydrogels (**Park et al., 2018**; **Stewart et al., 2018**; **Yun and Huang, 2016**), FDA-approved polymer miscellas – such as pegylated (PEG)-IFNα (**Foser et al., 2003**; **Glue et al., 2000**) – and IFNα cell/gene therapy approaches (**Catarinella et al., 2016**), which could quickly translate our results into clinical practice. Of note, the use of clinically approved doses of pegylated-IFNα has shown improved serum stability and clinical efficacy and reduced side effects, with serum IFNα concentrations similar to those achieved in our system (**Foser et al., 2003**; **Glue et al., 2000**).

All in all, the results of this study support the use of continuous low doses of IFNα as an antimetastatic drug during the perioperative period, due to its ability to transform a metastases-prone liver into a metastases-resistant organ.

Materials and methods

Animal studies

Eight- to 10-week-old C57BL/6 J and BALB/c mice were purchased from Charles River Laboratory, Calco, Italy. CB6 mice were obtained by crossing *Mus musculus* inbred C57BL/6 J male mice (H-2b restricted) with *Mus musculus* inbred BALB/c female mice (H-2d restricted), to produce H-2bxd F1 hybrids. *Ifnar1*$^{fl/fl}$ mice on a C57BL/6 J background (B6(Cg)-*Ifnar1*tm1.1Ees/J, JAX:028256), *Alb*^{Cre} (B6.Cg-Speer6-ps1Tg(*Alb*-cre)21Mgn/J, JAX:003574), *Pdgfrb*^{CreERT2} (B6.Cg-Tg(Pdgfrb-cre/ERT2)6096Rha/J JAX:029684), *Itgax*^{Cre} (CD11c, B6.Cg-Tg(*Itgax*-cre)1-1Reiz/J, JAX:008068), and Rosa26-ZsGreen (B6.Cg-Gt(ROSA)26Sortm6(CAG-ZsGreen1)Hze/J, JAX:007906) reporter mice were purchased from the Jackson Laboratory. *Cdh5*(PAC)$^{-CreERT2}$ mice (*VeCad*^{iCreERT2}) (**Wang et al., 2010**) were kindly provided by S. Brunelli (UniMib, Milan). NOD-scid IL2Rγnull (NSG) immunodeficient mice (NOD.Cg-Prkdcscid Il2rgtm1Wjl/SzJ, JAX:005557) and OT-I mice (C57BL/6-Tg(TcraTcrb)1100Mgb/Crl, JAX:003831) were purchased from Charles River Laboratory.

The conditional deletion of *Ifnar1* was obtained by crossing mice carrying loxP-flanked *Ifnar1* (**Prigge et al., 2015**) with transgenic mice expressing Cre recombinase under the control of either endothelial cell (*VeCad*^{iCreERT2}), stellate cell (*Pdgfrb*^{CreERT2}), hepatocyte (*Alb*^{Cre}) and dendritic cell (*Itgax*^{Cre}) promoters. To induce the Cre recombination and *Ifnar1* deletion into *VeCad*^{iCreERT2}, Cre recombinase was induced by three subcutaneous injections of Tamoxifen 50 mg/kg at p5, p6 and p7, as previously described (**Tirone et al., 2018**), while *Pdgfrb*^{CreERT2} adult mice were treated by three consecutive ip injections of Tamoxifen 100 mg/kg. Upon treatment, the exon3 of *Ifnar1* is excised resulting in a loss of *Ifnar1* in endothelial and stellate cells. To ensure that *Ifnar1* exon 3 of was efficiently excised hepatic DNA was isolated from the liver of 8-week-old *VeCad*^{Ifnar1_KO}, *Pdgfrb*^{Ifnar1_KO}, *Alb*^{Ifnar1_KO} and *Itgax*^{Ifnar1_KO} mice and polymerase chain reaction (PCR) analysis using *Ifnar1* intron 3-forward and *Ifnar1* intron 3-reverse oligonucleotides was performed. To control for possible changes in the microbiota composition of *VeCad*^{Ifnar1_KO}, *Pdgfrb*^{Ifnar1_KO}, *Alb*^{Ifnar1_KO} and *Itgax*^{Ifnar1_KO} and *Ifnar1*$^{fl/fl}$ littermates, mice from each litter and cage were randomly allocated into the experimental groups and were co-housed or systematically exposed to beddings of the other groups to ensure the same exposure to the microbiota.

Study approval

All animal experiments were approved by the Animal Care and Use Committee of the San Raffaele Scientific Institute (SRSI, IACUC 691, 808 and 1042) and were conducted in specific pathogen-free (SPF) facility in microisolator cages under a 12 hr light/dark cycle with free access to water and standard mouse diet (Teklad Global 18% Protein Rodent Diet, Harlan).

CRC cell lines

CT26 (H-2d, BALB/c-derived) cell line was purchased from ATCC. MC38 (H-2b, C57BL/6-derived), have been previously described (**Catarinella et al., 2016**). MC38 cells were transduced with a PGK-GFP lentiviral vector, cloned and sorted by FACS to establish MC38^{GFP} fluorescently tagged cell lines (**Talamini et al., 2021**). All cells were routinely tested for mycoplasma contamination using the

N-GARDE Mycoplasma PCR reagent set (EuroClone). CT26 and $CT26^{LM3}$ cells were cultured under standard condition at 37 °C in a humid atmosphere with 5% CO_2 in RPMI GlutaMAX medium (Gibco) supplemented with 10% FBS (Lonza) and 1% penicillin/streptomycin (P/S) (Gibco). MC38, $MC38^{GFP}$, $MC38^{Ifnar1_KO}$ and cells were cultured under standard condition at 37 °C in a humid atmosphere with 5% CO_2 in DMEM GlutaMAX medium (Gibco) supplemented with 10% FBS (Lonza) and 1% P/S (Gibco). Cell number and dimension was routinely assessed by automated CytoSMART cell counter (Corning). Details of murine cell lines used in the experiments (source of cell lines, background and origin of cancer) are mentioned in key resource table. The tumor cell lines MC38, $MC38^{GFP}$, $MC38^{Ifnar1_KO}$ and CT26 were passaged in vivo once before use in experiments.

Mouse models of liver metastases

Eight-to ten-week-old sex- and age-matched mice were injected with $5x10^3$ CT26 or $5x10^4$ MC38 CRC cell lines either through intrasplenic or superior mesenteric vein injections as previously described (***Catarinella et al., 2016***; ***van der Bij et al., 2010***). For early time point experiments, $7x10^5$ $MC38^{GFP}$ cells were injected in the superior mesenteric vein of anesthetized mice as described (***van der Bij et al., 2010***). For intrasplenic or superior mesenteric vein injections, deep anesthesia was induced by isoflurane inhalation (5% induction and 2% for maintenance in 2 l/min oxygen). The indicated number of CRC cells was injected into spleen or the superior mesenteric vein using a 29 G needle and to prevent excessive bleeding vein puncture was compressed with a sterile and absorbable hemostatic gauze (TABOTAMP). The peritoneum and skin were sutured with silk 4.0 and 7 mm wound clips as described (***Catarinella et al., 2016***). This experimental setting may mimic the vascular spreading of CRC cells during primary tumor resection and, thus, preventive IFNα infusion may be considered as a neoadjuvant treatment.

Mouse model of orthotopic colorectal cancer liver metastases

The generation of highly metastatic CT26 CRC cells was obtained by three consecutive rounds of in vivo selection as previously reported (***Zhang et al., 2013***). Briefly, $2x10^6$ CT26 cells were first injected subcutaneously into the right flank of immunodeficient NSG mice. After 28 days, tumors were excised, dissected, sliced into small fragments, and digested for 30 min at 37 °C in DMEM containing collagenase type IV (200 units/ml; Sigma-Aldrich) and Dnase I (100 units/ml; Sigma-Aldrich). The resulting cell suspension defined as $CT26^{sc}$, were maintained at 4 °C, filtered through a 70 µm nylon cell strainer (BD Biosciences, Bedford, MA), washed in PBS, and grown in RPMI 10% FBS. Sub-confluent $CT26^{sc}$ cells were harvested, resuspended in PBS:Matrigel (1:1) (Corning, MERK) and then injected into the cecal wall of immune competent anesthetized (isoflurane, 5% induction and 2% for maintenance in 2 l/min oxygen), CB6 recipient mice as described (***Zhang et al., 2013***). Briefly, a midline incision was made to exteriorize the cecum. Using a 33 G micro-injector (Hamilton, USA), 10 µl of a 50% Matrigel solution (BD Bioscience, USA) containing $2x10^5$ $CT26^{sc}$ cells were injected into the cecum wall. To avoid intraperitoneal spreading of $CT26^{sc}$, the injection site was sealed with tissue adhesive (3 M Vetbond, USA) and washed with 70% alcohol. The cecum was replaced in the peritoneal cavity, and the abdominal wall and skin incision was sutured with silk 4.0 and 7 mm wound clips as described (***Catarinella et al., 2016***). Twenty-eight days after injection, mice were euthanized and single cell suspensions of liver metastatic lesions, defined as $CT26^{LM1}$, were obtained as described above. This cycle was repeated twice to obtain the highly metastatic $CT26^{LM3}$ cells.

Recombinant mouse IFNα therapy

Continuous intraperitoneal IFNα delivery (IFNα1 carrier-free, Biolegend, San Diego, CA, USA) was achieved by intraperitoneal implantation of mini-osmotic pumps (MOP, ALZET, Cupertino, CA, USA) able to deliver either 50, 150, or 1050 ng IFNα a day for 14 or 28 days. NaCl-containing MOP were used as controls. Within each specific experiment, mice of each genotype were randomly assigned to receive either NaCl- or IFNα-containing MOP. MOP filling, priming and implantation within the peritoneum was performed following manufacturer's instructions. To avoid MRI artifacts due to the presence of metallic components within MOP, the day before MRI acquisition, MOP were removed from the peritoneum. To directly investigate responsiveness of liver cells to IFNα, signaling downstream of *Ifnar1* receptor was assessed by measuring pSTAT1 by IHC 30 min after an ip injection of NaCl or 1 µg IFNα, a dose able to synchronize pSTAT1 expression in all *Ifnar1* expressing cells (***Lin et al., 2016***).

Tumor rechallenge of IFNα cured mice

IFNα-cured mice that were designated as MC38-tumor free for at least 50 days after challenge, were subcutaneously rechallenged with $5x10^3$ MC38 cells resuspended in 200 µl of PBS:Matrigel (1:1). Age-matched naïve syngeneic mice were used as control. Tumor volumes were measured twice a week and euthanized for ethical reasons when tumor size reached ~500 mm^3.

Magnetic resonance imaging (MRI)

All MRI studies were carried out at the Experimental Imaging Center of SRSI on a preclinical 7-Tesla MR scanner (Bruker, BioSpec 70/30 USR, Paravision 6.0.1, Germany) equipped with 450/675 mT/m gradients (slew rate: 3400/4500 T/m/s; rise time 140 µs), coupled with a dedicated 4 channels volumetric mouse body coil. All images were acquired in vivo, under inhalational anesthesia (Isoflurane, 3% for induction and 2% for maintenance in 1 L/min oxygen) with mice laid prone on the imaging table. A dedicated temperature control system was used to prevent hypothermia; respiratory rate and body temperature were continuously monitored (SA Instruments, Inc, Stony Brook, NY, USA) during the whole MRI scan. An intravenous injection of gadoxetic acid (Gd-EOB-DTPA; Primovist, Bayer Schering Pharma) at a dose of 0.05 µmol/g of body weight was administered via the tail vein before placing the mice on the scanner table. As previously described (***Sitia et al., 2012***), the MRI studies relied on an axial fat-saturated T2-weighted sequence (TurboRARE-T2: TR = 3394ms, TE = 33ms, voxel-size=0.125 × 0.09 x0.8mm, averages = 3) acquired immediately after Gd-EOB-DTPA injection and an axial fat-saturated T1-weighted scan (RARE-T1: TR = 581ms, TE = 8.6ms, voxel-size=0.125 × 0.07 x0.8mm, averages = 4) acquired thereafter, during the hepatobiliary phase (HBP) of contrast excretion (starting from 10 min after Gd-EOB-DTPA injection). Two board certified radiologists skilled in clinical and preclinical abdominal MR imaging, blinded to any other information, reviewed all MRI studies using an open-source image visualization and quantification software (Mipav, 5.3.4 and later versions, Biomedical Imaging Research Services Section, ISL, CIT, National Institute of Health, USA). Liver metastases were identified as focal lesions showing slight hyper-intensity on T2-weighted images and concurrent hypo-intensity on contrast-enhanced HBP T1-weighted images. Liver metastases segmentation was performed by manual drawing of regions-of-interest (ROIs) on each slice, yielding volumes-of-interest (VOIs; lesion area x slice thickness) for the entire sequence. The total CRC metastatic mass was obtained by summing up the volumes of all single VOIs that were semi-automatically provided by the software.

MC38 gene editing

To knockout *Ifnar1* in MC38 cell line, we used GeneArt CRISPR Nuclease Vector with OFP Reporter Kit (ThermoFisher Scientific). Target-specific CRISPR RNA guides (crRNA) were designed using GeneArt CRISPR Search and Design Tool (ThermoFisher Scientific) and the two following crRNAs with the fewest predicted off-target effects were selected: crRNA1: TAGACGTCTATATTCTCAGGGTTTT; crRNA2: ATGTAGACGTCTATATTCTCGTTTT. Annealed crRNAs were cloned in GeneArt CRISPR Nuclease Vector with OFP according to the manufacturer's instructions and vector constructs were used to transform OneShot TOP10 chemically competent *E. coli* cells (ThermoFisher Scientific). Vectors were validated by Sanger sequencing of DNA from 10 colonies for each crRNA (LightRun GATC Carlo Erba). To express the CRISPR–Cas9 system transiently, 2 µg of each vector were used to transfect $5x10^5$ MC38 cell line with Lipofectamine 2000 (ThermoFisher Scientific) in Opti-MEM medium (ThermoFisher Scientific). After 3 days, transfection efficiency was evaluated measuring the orange fluorescence protein (OFP) by FACS (LSRFortessa) and data analysed using FlowJo v10.5. OFP positive bulk populations were single-cell cloned in 96-well plates and a total of 12 clones screened for mismatches by T7E1 assay (New England Biolabs). Briefly, genomic DNA from MC38 clones was extracted by Qiamp mini kit (Qiagen) and amplified within the exon 2 of *Ifnar1* locus using the following oligos: *Ifnar1* exon2 forward, TCCAAGACTCCTGCTGTC and *Ifnar1* exon2 reverse: GCACTTTTACTTGCTC GGT. The PCR products were denaturated and annealed according to manufacture protocol (New England Biolabs). The digestion reaction was run onto 2% agarose gel to identify mismatched clones. Genetic validation of T7E1-positive clones was assessed by cloning the PCR products with TOPO TA Cloning, Dual Promoter, Kit (ThermoFisher Scientific) and subsequently 10 clones per cell line were sequenced (LightRun GATC Carlo Erba). Functional validation of *Ifnar1* knockout MC38 cells was

determined by RT-PCR for the ISG *Irf7* after 4 hr of in vitro stimulation with 300 ng/ml IFNα, using MC38 transfected non-edited WT clone as control (MC38).

Peripheral blood analyses

At the indicated time points after IFNα administration, whole anti-coagulated blood of MOP-NaCl and MOP-IFNα-treated mice was collected from the retro-orbital plexus of anesthetized animals (isoflurane, 5% for induction and 2% for maintenance in 2 l/min oxygen) using Na-heparin coated capillaries (Hirschmann Laborgeräte GmbH, Germany) and vials (Microvette, Sarstedt, Germany). Hematologic parameters were evaluated using an automated cell counter (ProCyte Dx, IDEXX Laboratories, USA). The extent of hepatocellular injury was monitored by measuring serum ALT (sALT) activity at several time points after IFNα treatment, as previously described (***Sitia et al., 2012***).

Measurement of plasma IFNα by ELISA

Circulating levels of IFNα were quantified in plasma collected from NaCl controls or IFNα-treated mice at indicated time points using VeriKine-HS Mouse IFNα all Subtype ELISA Kit (PBL) according to the manufacturer's instructions. The IFNα titer in the samples was determine by plotting the optical density (OD) subtracted of blank OD to eliminate background, using a 4-parameter logistic fit for the standard curve by using Prism v8 (GraphPad). Detection range is comprised between 2.38 and 152 pg/ml of IFNα.

RNA extraction and quantitative real-time PCR gene expression analyses

Total RNA was isolated from liver homogenates of MOP-NaCl control and MOP-IFNα-treated mice by using the ReliaPrep RNA Tissue Miniprep System (Promega) and DNAse TURBO (Thermo Fisher Scientific) following manufacturer's recommendation. The extracted RNA was subsequently retro-transcribed to cDNA as previously described (***Sitia et al., 2011***). Quantitative real-time PCR analysis was performed utilizing the ViiA7 Fast Real-Time PCR System (Applied Biosystems). The ISG, *Irf7* (Mm00516793_g1) as well as the housekeeping *Gapdh* (Mm 99999915_g1) were quantified by using the indicated FAM-MGB labeled TaqMan Gene Expression Assays (Applied Biosystems). Gene expression was determined as the difference between the threshold cycle (Ct) of the gene of interest (Goi) and the Ct of the housekeeping (*Gapdh*) of the same sample (ΔCt). The fold-change expression of each Goi was calculated over its basal expression in the control sample by the formula $2^{-\Delta\Delta Ct}$ as described (***Sitia et al., 2012***).

Immunohistochemistry

At time of autopsy for each mouse, livers were perfused with PBS, harvested and different pieces were sampled, fixed in zinc-formalin, processed and embedded in paraffin for histological and immunohistochemical analysis, as previously described (***Sitia et al., 2012***). Immunohistochemical staining using a Bond RX Automated Immunohistochemistry (Leica Microsystems GmbH, Wetzlar, Germany) was performed on 3-µm-thick sections. First, tissues were deparaffinized and pre-treated with the Epitope Retrieval Solution [ER1 Citrate Buffer for Ki-67 (dilution 1:200, clone SP6, Thermo Fisher Scientific) and F4/80 (dilution 1:200, clone A3-1, Bio-Rad); ER2 EDTA for CD3 (dilution 1:100, clone SP7, Abcam),CD34 (dilution 1:300, clone MEC14.7, Biolegend) and pSTAT1 (dilution 1:800, clone 58D6, Cell Signaling)] at 100 °C for 30 min. After washing steps, peroxidase blocking was carried out for 10 min using the Bond Polymer Refine Detection Kit DS9800 (Leica Microsystems GmbH). Then, tissues were washed and incubated for 1 hr RT with the primary antibody diluted in IHC Antibody Diluent (Novocastra, Leica RE7133). Subsequently, tissues were incubated with polymer-HRP or Rat-on-Mouse HRP (Biocare Medical, RT517H), developed with DAB-Chromogen for 10 min and counter-stained with Hematoxilin for 5 min. For image acquisition and analysis, eSlide Manager (Aperio Leica Biosystems) was used. All images were acquired using the Aperio AT2 system (Leica Biosystems). Quantifications were performed by automated image analysis software through dedicated macros of the ImageScope program, customized following manufacturer's instructions (Leica Biosystems). The images shown were identified as representative area of interest within the total area of the specimen analyzed and exported as ImageScope snapshots.

Immunofluorescence and confocal microscopy

Livers were perfused with PBS, harvested and fixed over-night in 4% paraformaldehyde (PFA), equilibrated in 30% sucrose in PBS over-night at 4 °C prior to embedding in OCT (Bio-Optica) for quick freezing at –80 °C. Thirty-µm-thick cryosections were adhered to Superfrost Plus slides (Thermo Scientific). For immunofluorescence staining, sections were blocked and permeabilized with PBS containing 5% FBS and 0.1% Triton X-100 (Sigma-Aldrich) for 30 min at room temperature and subsequently incubated with 10% of donkey serum (DS; Sigma-Aldrich) in PBS for 30–60 min at room temperature. Staining with primary and secondary antibodies, were performed with staining buffer (PBS with 1.5% DS, 0.2% Triton X-100 and 1% BSA), using the following antibodies and dilutions: anti-PDGFRβ/CD140b (dilution 1:200, clone APB5, eBioscience)+anti rat AF647 (dilution 1:200, Jackson IR); anti-CD11c AF647, (dilution 1:100, clone N418, Biolegend); anti-GFP (dilution 1:100, rabbit polyclonal, A11122 Thermo Fisher Scientific)+anti-rabbit AF 488 (dilution 1:200, Thermo Fisher Scientific); anti-CD31/PECAM-1 (dilution 1:300, goat polyclonal, AF3628 R&D Systems)+anti goat AF546 (dilution 1:200, Thermo Fisher Scientific); anti-Heparan Sulfate (dilution 1:50, clone F58-10E4, Amsbio)+anti IgM conjugated to APC (dilution 100, clone II/41, Thermo Fisher Scientific); anti-LYVE-1 (dilution 1:300, rabbit polyclonal, Novus Biologicals)+anti-rabbit AF647 (dilution 1:200, Thermo Fisher Scientific); anti-Collagen type IV (dilution 1:100, rabbit polyclonal, Abcam)+anti-rabbit AF488 (dilution 1:200, Thermo Fisher Scientific); anti-Laminin (dilution 1:300, rabbit polyclonal, Sigma-Aldrich)+anti-rabbit AF488 (dilution 1:200, Thermo Fisher Scientific); anti-CD54/ICAM1 (dilution 1:100, clone YN1/1.7.4, Biolegend)+anti rat AF647 (dilution 1:200, Jackson IR); anti-CD62E/E-selectin (dilution 1:100, clone 10E9.6, BD Bioscience)+anti rat AF647 (dilution 1:200, Jackson IR). Confocal images were acquired using a Leica SP8 confocal systems (Leica Microsystems) that are available at the SRSI Advanced Light and Electron Microscopy BioImaging Center (ALEMBIC). Fifteen–20 µm z-stacks were projected in 2D and processed using Fiji image processing software (***Schindelin et al., 2012***). Localization of $MC38^{GFP}$ tumor cells within liver vessels, 20–30 square xy sections (1024x1,024 pixel) confocal xyz stacks, from NaCl- and IFNα-treated mice, were acquired with 0.5 µm z-spacing on a Leica TCS SP8. The Imaris Surpass View and Surface Creation Wizard were used to create 3D renderings of $MC38^{GFP}$ cells and $CD31^{+}$ liver vessels as previously reported (***Guidotti et al., 2015***). A tumor cell was considered intravascular when at least 95% of its surface-reconstructed body was inside the vessel lumen in all the acquired sections projected in the horizontal (xy), transversal (yz) and longitudinal (xz) planes. Entire liver sections were acquired using MAVIG RS-G4 confocal microscope (MAVIG GmbH Research, Germany) to quantify the number of $MC38^{GFP}$ tumor cells in relation to the total liver area. The quantification of the percentage of liver area covered by endothelial markers and extracellular matrix components, such as Heparan Sulfate, Laminin, Collagen type IV, ICAM1 and E-Selectin, was evaluated using ImageJ software, applying the same threshold to the different experimental groups for each channel and measuring the percentage of area limited to threshold. Colocalization analysis of GFP in the different Cre recombinant mouse models was performed using an unsupervised ImageJ plugin algorithm termed Colocalization, which was developed by Pierre Bourdoncle (Institut Jacques Monod, Service Imagerie, Paris; 2003–2004).

Scanning and transmission electron microscopy

Electron microscopy (EM) fixative composition was 2,5% glutaraldehyde, 2% paraformaldehyde, 2 mM $CaCl_2$ and 2% sucrose in 0.1 M Na cacodylate buffer (pH 7,4). For the analysis of endothelial GCX, the EM fixative was supplemented with 2% Lanthanum nitrate (MERK) as previously reported (***Inagawa et al., 2018***). Warm PBS and EM fixative at 35–37°C was used to ensure tissue integrity. When mice were under deep anesthesia, with a single ip injection of 50–60 mg/kg Tribromoethanol (Avertin), a Y incision was made in the abdomen to expose the liver and the portal vein. The portal vein was cannulated with an appropriately sized IV cannula of 22 G and the liver was perfused with 15 ml of warm PBS at a constant rate of 3 rpm using a peristaltic pump (Peri-Star Pro, 2Biological Instruments) as previously reported (***Guidotti et al., 2015***). In situ fixation was achieved by perfusing EM fixative for approximately 5 min at 3 rpm. Fixed liver was harvested and cut into 5 mm blocks using a scalpel. Liver blocks were ulteriorly immersed in EM fixative for 24–72 hr at 4 °C and finally EM fixative was replaced with 0.1 M sodium cacodylate buffer and stored at 4 °C until processed for TEM or SEM analysis. Liver blocks were post-fixed in 1% osmium tetroxide (OsO_4), 1,5% potassium ferricyanide($K_4[Fe(CN)_6]$) in 0.1 M Na Cacodylate buffer for 1 hr on ice. Afterwards, for SEM, 150-µm-thick

sections were obtained from perfused livers using a vibratome (Leica VT1000S). Sections were further post-fixed in 1% OsO_4 in 0.1 M Na Cacodylate, dehydrated through a series of increasing concentration of ethanol and immersed in absolute hexamethyldisilazane (HMDS) that was left to evaporate overnight. Dried sections were sputter-coated with Chromium using a Quorum Q150T ES sputter coater. Sections were then mounted on SEM stubs using conductive adhesive tape and observed in a field-emission scanning electron microscope Gemini 500 (ZEISS, Oberkochen, Germany). The LSEC fenestra measurements were performed from SEM microphotographs taken under a magnification of 20,000 X, using three independent samples from each experimental condition [NaCl-*Ifnar1*$^{fl/fl}$ (n=3), IFNα-*Ifnar1*$^{fl/fl}$ (n=3), NaCl-*VeCad*^{Ifnar1_KO} (n=3) and IFNα-*VeCad*^{Ifnar1_KO} mice (n=3)] and a total area of about 720 µm^2 of sinusoids was analyzed for each mouse. After 40 days of IFNα discontinuation, two randomly selected liver micrographs of IFNα-*Ifnar1*$^{fl/fl}$ (n=3) were analyzed to determine LSEC fenestra measurements and a total area of approximately 300 µm^2 of sinusoidal surface was analyzed. All measurements were made using the ImageJ software, as previously described (***Cogger et al., 2015***). Briefly, the flattened area of the liver sinusoid was selected and longest diameter of each fenestrae was measured. Gaps larger than 250 nm were excluded from the analysis. The average fenestration diameter (defined as the average of all fenestrae diameters excluding gaps area), the fenestration area (π r2, where r, the radius, was calculated from the individual fenestrae diameter *r*=d/2, without gaps area), the porosity [Σ(π r2)/(total area analyzed – Σ(area of gaps))×100; expressed as a percentage], and the fenestration frequency [total number of fenestrations/(total sinusoidal area analyzed – Σ(area of gaps)); expressed as µm2] have been calculated. Surface roughness analysis of endothelial GCX was determined using Image J software. The flattened area of the liver sinusoid was analyzed, with the SurfChartJ1Q plugin to determine the roughness deviation of all points from a plane after background subtraction, known as Ra coefficient, as previously reported (***Pavlović et al., 2012***). A representative area within the flatten liver sinusoidal surface was used to generate a 3D surface plot image.

For TEM, tissue pieces were rinsed in Na Cacodylate buffer, washed with distilled water (dH2O) and en bloc stained with 0.5% uranyl acetate in dH_2O overnight at 4 °C in the dark. Finally, samples were rinsed in dH_2O, dehydrated with increasing concentrations of ethanol, embedded in Epon resin and cured in an oven at 60 °C for 48 hr. Ultrathin sections (70–90 nm) were obtained using an ultramicrotome (UC7, Leica microsystem, Vienna, Austria), collected, stained with uranyl acetate and Sato's lead solutions, and observed in a Transmission Electron Microscope Talos L120C (FEI, Thermo Fisher Scientific) operating at 120kV. Images were acquired with a Ceta CCD camera (FEI, Thermo Fisher Scientific). TEM microphotographs were taken under a magnification of 3.400 X, using three independent samples from each experimental condition and a total area of approximately 2.575 µm^2 was analyzed for each mouse. LSECs thickness and the width of the space of Disse were measured using ImageJ software. For collagen deposition analysis, at least 10 randomly selected sinusoids from each mouse were analyzed as previously reported (***Gissen and Arias, 2015***; ***Warren et al., 2007***).

Isolation of liver non-parenchymal cells (NPCs)

Liver NPCs, including leukocytes, were isolated from NaCl control or IFNα-treated mice 7 days after MOP implantation, as previously described (***Bénéchet et al., 2019***). Briefly, after euthanasia, the liver was perfused through the vena cava with 5–8 ml of PBS to remove most blood cells. Livers were weighted and 50% of the tissue was sliced in small pieces and incubated 30 min at 37 °C in 10 ml of digestion medium (RPMI GlutaMAX medium [Gibco] containing 200 U/ml of collagenase type IV [Sigma-Aldrich] and 100 U/ml of DNAse I [Sigma-Aldrich]). Remaining undigested fragments were syringed with an 18 G needle and filtered through a 70 µm cell strainer to obtain a single cell suspension. Cells were centrifuged 3 min at 50 g at room temperature and the pellet containing hepatocytes was discarded. The resultant cell suspension of NPCs was incubated for 30 s with ACK lysis buffer (Lonza) to deplete red blood cells, washed with cold RPMI. NPCs were counted and processed for flow cytometry analysis or sorting.

Isolation of splenocytes and naïve CD8$^+$ T cells

Spleens were obtained from *Ifnar1*$^{fl/fl}$ and *VeCad*^{Ifnar1_KO} mice 21 days after MC38 cells challenge and placed in a 70 µm cell strainer on a petri dish containing 10 ml of plain RPMI, ground with a syringe plunger to obtain a cell suspension and washed three times with plain RPMI as previously described (***Sitia et al., 2012***). The cell suspension was centrifugated at 400 g for 5 min at room temperature, the

resuspended pellet was incubated for 30 s with ACK lysis buffer and neutralized with RPMI. Resultant splenocytes were counted and processed for FACS analysis. Splenocytes derived from OT1 mice were prepared as described above and naïve $CD8^+$ T cells were isolated using EasySep Mouse Naïve $CD8^+$ T cell isolation kit (STEMCELL Technologies) following manufacturer's instructions.

Flow cytometry and cell sorting

Cells were resuspended in PBS and LIVE/DEAD Fixable Near-IR or Green dead cell dyes (Thermo Fisher Scientific) and incubated 15 min at RT in the dark for cell viability assessment. Subsequently, cells were blocked with FACS buffer (PBS supplemented with 2% FBS) containing InVivo Mab anti-mouse CD16/CD32 (BioXCell) and stained for surface markers using the following antibodies: anti-CD45R/B220 (clone RA3-6B2, Biolegend), anti-CD11b (clone M1/70, Biolegend), anti-mouse CD11c (clone N418, Biolegend), anti-CD3 (clone 145–2 C11, Thermo Fisher Scientific), anti-CD45 (clone 30-F11, Bioegend), anti-CD8a (clone 53–6.7, Biolegend), anti-F4/80 (clone BM8, Biolegend), anti-CD126/IL-6RA (clone D7715A7, Biolegend), anti-CD18/ITGB2 (clone M18/2, Biolegend), anti-CD49d/ITGA4 (clone 9C10(MFR4.B), Biolegend), anti-H-2Kb/H-2Db (clone 28-8-6, Biolegend), anti-CD86 (clone GL-1, Biolegend), anti-CD146 (clone ME-9F1, Biolegend), anti-CD44 (clone IM7, Biolegend), anti-CD62L (clone MEL-14, Biolegend), anti-IFNγ (clone XMG1.2, BD Biosciences), anti-CD31 (clone MEC13.3, BD Biosciences)for 20 min at 4 °C. For intracellular IFNγ staining, cells were then fixed, permeabilized and stained following Foxp3/Transcription Factor Staining buffer set (Thermo Fisher Scientific) manufacturer's guidelines. When preparing samples for FACS sorting, NPCs were directly blocked and stained with CD45-APC and CD31-BV421. Viability was evaluated by 7-AAD (Biolegend) staining that was added to samples 5 min before sorting. Cell sorting was performed on a BD FACSAria Fusion (BD Biosciences) equipped with four lasers: Blue (488 nm), Yellow/Green (561 nm), Red (640 nm) and Violet (405 nm). 85 µm nozzle was used and sheath fluid pressure was at 45 psi. A highly pure sorting modality (four-way purity sorting) was chosen. The drop delay was determined using BD FACS AccuDrop beads. Unstained and a single-stained controls have been used to set up compensation. Rainbow beads (SPHEROTM Rainbow Calibration Particles) were used to standardize the experiment and were run before each acquisition. Samples were sorted at 4 °C to slow down metabolic activities. Sorted cells were collected in 1.5 ml Eppendorf tubes containing 200 µl of DMEM 10% FBS medium and immediately processed for RNA extraction using ReliaPrep RNA Cell Miniprep System (Promega) and DNAse TURBO (Thermo Fisher Scientific) following manufacturer's recommendation.

Isolation of HECs, including LSECs and splenic DCs for in vitro studies

Mouse liver perfusion was performed as described in the section Electron Microscopy. After PBS perfusion, liver digestion was achieved in situ by perfusing warm digestion medium at 4 rpm for 10 min. The cava vein was squeezed tight several times to build up some pressure within the liver in order to fill all liver lobes with digestion medium. The resultant digested liver was excised, placed on a petri dish containing digestion medium and the Glisson's capsule was removed. Disaggregated tissue was filtered using a 70-µm cell strainer and centrifuged at 50 g for 3 min to discard hepatocytes. The supernatant containing NPCs was counted and Kupffer cells (KC) were removed using anti-F4/80 Ultrapure microbeads (Miltenyi Biotec) following manufacturer's guidelines. The flow-through of unlabeled NPCs was placed on top of a 25–50% Percoll gradient and centrifuged at 850 g for 20 min at RT without brake and the LSECs located at the 25/50% interface were collected. LSECs were counted and 10^5 cells were seeded in a 48-well plate and cultured in collagenated plates with EGM-2 medium (Lonza) for 3 days. For the isolation of splenic DC, spleens were slowly injected with 1 ml of digestion medium until they changed from dark maroon to reddish-orange color. Then, the spleen was minced and pipetted vigorously several times in digestion medium. The cell suspension was filtered using a 70 µm cell strainer, and larger undigested fragments were ulteriorly incubated with digestion medium at 37 °C for 30 min. After tissue digestion, splenocytes were centrifuged at 500 g for 5 min and washed three times with plain RPMI supplemented with 5 mM EDTA to disrupt DC-T cell complexes. Red blood cells were lysed with ACK lysis buffer and DCs cells were isolated using anti-CD11c microbeads UltraPure (Miltenyi) according to manufacturer's instructions. $CD11c^+$ DCs were counted and seeded at 10^5 cells in a 48-well plate using RPMI GlutaMAX supplemented with 10% FBS, 1% P/S, 1 x Na Pyruvate (Gibco), 1 x MEM Non-essential Amino Acid Solution (Gibco), 20 µM

β-mercaptoethanol and 40 ng/ml GM-CSF (BioXcell). Every 48 hr 200 µl of fresh medium were added to cultured cells and DCs were grown for 7 days to stimulate DCs differentiation.

Antigen cross-priming

Prior to naïve $CD8^+$ T cell co-culture, HECs, including LSECs, and sDCs were stimulated for 18 hr with 1 µg/ml of SIINFEKL peptide (OVA 257–264, Proimmune) or with 1 mg/ml of low endotoxin soluble ovalbumin protein (sOVA; Sigma-Aldrich) in combination with NaCl or 5 ng/ml of IFNα. Subsequently, after extensive washes, cells were co-culture with $5x10^5$ naive $CD8^+$T cells isolated from OT-I mice in complete RPMI (containing 10% FBS and 50 µM β-mercaptoethanol) in combination with NaCl or 5 ng/ml of IFNα. After 3 days, $CD8^+$ T cells were stimulated for 4 hr with 1 µg/ml of SIINFEKL peptide, 5 µg/ml of Brefeldin A (Sigma-Aldrich) and 2.5% EL-4 supernatant in complete RPMI. Finally, the production of IFNγ and the expression of activation markers, such as CD44, were measured by FACS.

RNA-seq and bioinformatic data analysis

RNA integrity, isolated from sorted liver $CD31^+$ cells, was evaluated using the Agilent 4100 TapeStation (Agilent Technologies) and samples with RNA integrity number (RIN) above 7.0 were used for subsequent RNA-Seq-based profiling. Libraries were prepared using the Illumina Stranded mRNA ligation kit, according to the manufacturer's instructions. The RNA-Seq library was generated following the standard Illumina RNA-Seq protocol and sequenced on an Illumina NovaSeq 6000 machine (Illumina, San Diego, CA) obtaining an average of 40 millions of single-end reads per sample. The raw reads produced from sequencing were trimmed using Trimmomatic, version 0.32, to remove adapters and to exclude low-quality reads from the analysis. The remaining reads were then aligned to the murine genome GRCm38 using STAR, version 2.5.3 a. Reads were eventually assigned to the corresponding genomic features using featureCounts, according to the Gencode basic annotations (Gencode version M22). Quality of sequencing and alignment was assessed using FastQC, RseQC, and MultiQC tools. Expressed genes were defined as those genes showing at least 1 Count Per Million reads (CPM) on at least a selected number of samples, depending on the size of the compared groups (***Chen et al., 2016***). Low-expressed genes that did not match these criteria were excluded from the corresponding dataset. Gene expression read counts were exported and analyzed in R environment (v. 4.0.3) to identify differentially expressed genes (DEGs), using the DESeq2 Bioconductor library (v. 1.30.1, ***Love et al., 2014***). P-values were adjusted using a threshold for false discovery rate (FDR)<0.05 (***Benjamini and Hochberg, 1995***). Significant genes were identified as those genes showing FDR <0.05. Functional enrichment analysis was conducted using the enrichR R package (v. 3.0, ***Kuleshov et al., 2016***), starting from the lists of differentially expressed genes as defined by FDR <0.05. Selected pathways were grouped and summarized according to their general biological functions and the hypergeometric test was performed to test the enrichment of these custom genesets, exploiting the hypeR R package (v. 1.8.0). Pre-ranked Gene Set Enrichment Analysis (GSEA ***Subramanian et al., 2005***) was performed for each DGE comparison, on all the expressed genes ranked for Log2 fold change. The gene-sets included in the GSEA analyses were obtained from Canonical Pathways, Hallmark and the Gene Ontology collections as they are reported in the MsigDB database.

Statistical analysis

In all experiments, values are expressed as mean values ± SEM. Statistical significance was estimated by two-tailed non-parametric Mann-Whitney test (e.g. to evaluate differences generated as a consequence of tumor growth) or by one-way ANOVA with Tukey's multiple comparison test when more than two groups were analyzed. Contingency tables were tested by two-tailed Fisher's exact test and Chi-square test. Statistical significance of survival experiments was calculated by log-rank/Mantel-Cox test. All statistical analyses were performed with Prism 8 (GraphPad Software) and were reported in Figure legends. p-values <0.05 were considered statistically significant and reported on graphs. If not mentioned, differences were not statistically significant.

Acknowledgements

The authors thank B Mendicino, C.B. Ekalle-Soppo, E Daoud, P Giangregorio, M Nicoloso, M Raso, A Fiocchi, P Marra, T Canu, D Lazarevic, E Capitolo, S Bianchessi, V Berno, A Raimondi, A Loffreda, T Catelani, M Mainetti and P Di Lucia for technical support; M Silva for secretarial assistance, C

Tacchetti, P Dellabona and all the San Raffaele AIRC 5X1000 team for helpful discussion. SV Kotenko for help with pSTAT1 IHC protocol. Confocal immunofluorescence histology and electron microscopy was carried out at Alembic, an advanced microscopy laboratory established by the San Raffaele Scientific Institute and the Vita-Salute San Raffaele University. The use of Imaris software was provided by M Iannacone. Acquisition of SEM images was carried out at the Interdepartmental Microscopy Platform of the University of Milan Bicocca. Flow cytometry was carried out at FRACTAL, a flow cytometry resource and advanced cytometry technical applications laboratory established by the San Raffaele Scientific Institute. FRACTAL is an ISO 9001 certified facility and as such all the instruments and equipment are subject to a strict maintenance and functionality check plan. NLT is the recipient of a Swiss National Science Foundation Fellowship P2GEP3_171976; VB is the recipient of a Fondazione Umberto Veronesi "Post-doctoral Fellowships 2019"; AM is the recipient of a Francesco Fronzaroli Memorial fellowship and conducted this study as partial fulfilment of his PhD in Molecular Medicine within the program in Basic and Applied Immunology and Oncology at Vita-Salute San Raffaele University. LGG is supported by the Italian Association for Cancer Research (AIRC) Grant 22737, Lombardy Open Innovation Grant 229452, PRIN Grant 2017MPCWPY from the Italian Ministry of Education, University and Research, Funded Research Agreements from Gilead Sciences and Avalia Therapeutics; GS is supported by Italian Association for Cancer Research (AIRC) grants 18468, 22820 and AIRC 5 per Mille, grant 22737.

Additional information

Competing interests

Luca G Guidotti: LGG is a member of the board of directors at Genenta Science and Epsilon Bio and participates in advisory boards/consultancies for Gilead Sciences, Roche, Arbutus Biopharma and Antios Therapeutics. The other authors declare that no competing interests exist.

Funding

Funder	Grant reference number	Author
Associazione Italiana per la Ricerca sul Cancro	22737	Luca G Guidotti Giovanni Sitia
Associazione Italiana per la Ricerca sul Cancro	18468	Giovanni Sitia
Associazione Italiana per la Ricerca sul Cancro	22820	Giovanni Sitia
Regione Lombardia	229452	Luca G Guidotti
Ministero dell'Istruzione, dell'Università e della Ricerca	2017MPCWPY	Luca G Guidotti

The funders had no role in study design, data collection and interpretation, or the decision to submit the work for publication.

Author contributions

Ngoc Lan Tran, Conceptualization, Validation, Investigation, Visualization, Methodology, Writing – original draft; Lorena Maria Ferreira, Blanca Alvarez-Moya, Conceptualization, Validation, Investigation, Visualization, Methodology, Writing – original draft, Writing – review and editing; Valentina Buttiglione, Investigation, Visualization, Methodology; Barbara Ferrini, Paola Zordan, Andrea Monestiroli, Claudio Fagioli, Investigation, Methodology; Eugenia Bezzecchi, Giulia Maria Scotti, Data curation, Methodology; Antonio Esposito, Resources, Supervision; Riccardo Leone, Chiara Gnasso, Methodology; Andrea Brendolan, Resources, Methodology; Luca G Guidotti, Resources, Funding acquisition, Writing – review and editing; Giovanni Sitia, Conceptualization, Resources, Formal analysis, Supervision, Funding acquisition, Validation, Investigation, Visualization, Methodology, Writing – original draft, Project administration, Writing – review and editing

Author ORCIDs
Ngoc Lan Tran http://orcid.org/0000-0003-4270-376X
Lorena Maria Ferreira http://orcid.org/0000-0002-4262-0406
Blanca Alvarez-Moya http://orcid.org/0000-0003-2573-7909
Paola Zordan http://orcid.org/0000-0001-6915-5535
Andrea Monestiroli http://orcid.org/0000-0001-5818-2028
Claudio Fagioli http://orcid.org/0000-0001-9889-4695
Eugenia Bezzecchi http://orcid.org/0000-0002-8838-4736
Chiara Gnasso http://orcid.org/0000-0001-8005-5439
Andrea Brendolan http://orcid.org/0000-0003-0109-6879
Luca G Guidotti http://orcid.org/0000-0002-0205-2678
Giovanni Sitia http://orcid.org/0000-0003-1024-9128

Ethics

All animal experiments were approved by the Animal Care and Use Committee of the San Raffaele Scientific Institute (IACUC 691, 808 and 1042) and were conducted in specific pathogen-free (SPF) facility in microisolator cages under a 12-hour light/dark cycle with free access to water and standard mouse diet (Teklad Global 18% Protein Rodent Diet, Harlan).

Decision letter and Author response

Decision letter https://doi.org/10.7554/eLife.80690.sa1
Author response https://doi.org/10.7554/eLife.80690.sa2

Additional files

Supplementary files

- Transparent reporting form

Data availability

Sequencing data have been deposited in the Gene Expression Omnibus (GEO) database under the accession number GSE186203 for intrahepatic CD31 bulk RNA-seq. All data generated or analyzed during this study are included in the manuscript and supporting files.

The following dataset was generated:

Author(s)	Year	Dataset title	Dataset URL	Database and Identifier
Ferreira LM, Alvarez-Moya BA, Bezzecchi E, Scotti GM, Sitia G	2021	Continuous sensing of IFNα by hepatic endothelial cells shapes a vascular antimetastatic barrier	https://www.ncbi.nlm.nih.gov/geo/query/acc.cgi?acc=GSE186203	NCBI Gene Expression Omnibus, GSE186203

References

Aichele P, Unsoeld H, Koschella M, Schweier O, Kalinke U, Vucikuja S. 2006. Cd8 T cells specific for lymphocytic choriomeningitis virus require type I IFN receptor for clonal expansion. *Journal of Immunology* **176**:4525–4529. DOI: https://doi.org/10.4049/jimmunol.176.8.4525, PMID: 16585541

Ananth AA, Tai L-H, Lansdell C, Alkayyal AA, Baxter KE, Angka L, Zhang J, Tanese de Souza C, Stephenson KB, Parato K, Bramson JL, Bell JC, Lichty BD, Auer RC. 2016. Surgical stress abrogates pre-existing protective T cell mediated anti-tumor immunity leading to postoperative cancer recurrence. *PLOS ONE* **11**:e0155947. DOI: https://doi.org/10.1371/journal.pone.0155947, PMID: 27196057

Argilés G, Tabernero J, Labianca R, Hochhauser D, Salazar R, Iveson T, Laurent-Puig P, Quirke P, Yoshino T, Taieb J, Martinelli E, Arnold D, ESMO Guidelines Committee. Electronic address: clinicalguidelines@esmo.org. 2020. Localised colon cancer: ESMO clinical practice guidelines for diagnosis, treatment and follow-up. *Annals of Oncology* **31**:1291–1305. DOI: https://doi.org/10.1016/j.annonc.2020.06.022, PMID: 32702383

Augustin G, Bruketa T, Korolija D, Milosevic M. 2013. Lower incidence of hepatic metastases of colorectal cancer in patients with chronic liver diseases: meta-analysis. *Hepato-Gastroenterology* **60**:1164–1168. DOI: https://doi.org/10.5754/hge11561, PMID: 23803379

Badia-Ramentol J, Linares J, Gómez-Llonin A, Calon A. 2021. Minimal residual disease, metastasis and immunity. *Biomolecules* **11**:130. DOI: https://doi.org/10.3390/biom11020130, PMID: 33498251

Baiocchini A, Del Nonno F, Taibi C, Visco-Comandini U, D'Offizi G, Piacentini M, Falasca L. 2019. Liver sinusoidal endothelial cells (lsecs) modifications in patients with chronic hepatitis C. *Scientific Reports* **9**:8760. DOI: https://doi.org/10.1038/s41598-019-45114-1, PMID: 31217430

Bakos O, Lawson C, Rouleau S, Tai LH. 2018. Combining surgery and immunotherapy: turning an immunosuppressive effect into a therapeutic opportunity. *Journal for Immunotherapy of Cancer* **6**:86. DOI: https://doi.org/10.1186/s40425-018-0398-7, PMID: 30176921

Bénéchet AP, De Simone G, Di Lucia P, Cilenti F, Barbiera G, Le Bert N, Fumagalli V, Lusito E, Moalli F, Bianchessi V, Andreata F, Zordan P, Bono E, Giustini L, Bonilla WV, Bleriot C, Kunasegaran K, Gonzalez-Aseguinolaza G, Pinschewer DD, Kennedy PTF, et al. 2019. Dynamics and genomic landscape of CD8+ T cells undergoing hepatic priming. *Nature* **574**:200–205. DOI: https://doi.org/10.1038/s41586-019-1620-6, PMID: 31582858

Benjamini Y, Hochberg Y. 1995. Controlling the false discovery rate: a practical and powerful approach to multiple testing. *Journal of the Royal Statistical Society* **57**:289–300. DOI: https://doi.org/10.1111/j.2517-6161.1995.tb02031.x

Blériot C, Ginhoux F. 2019. Understanding the heterogeneity of resident liver macrophages. *Frontiers in Immunology* **10**:2694. DOI: https://doi.org/10.3389/fimmu.2019.02694, PMID: 31803196

Bocci V. 1994. Pharmacology and side-effects of interferons. *Antiviral Research* **24**:111–119. DOI: https://doi.org/10.1016/0166-3542(94)90059-0, PMID: 7526785

Bolger AM, Lohse M, Usadel B. 2014. Trimmomatic: a flexible trimmer for illumina sequence data. *Bioinformatics* **30**:2114–2120. DOI: https://doi.org/10.1093/bioinformatics/btu170, PMID: 24695404

Böttcher JP, Schanz O, Garbers C, Zaremba A, Hegenbarth S, Kurts C, Beyer M, Schultze JL, Kastenmüller W, Rose-John S, Knolle PA. 2014. Il-6 trans-signaling-dependent rapid development of cytotoxic CD8+ T cell function. *Cell Reports* **8**:1318–1327. DOI: https://doi.org/10.1016/j.celrep.2014.07.008, PMID: 25199826

Boukhaled GM, Harding S, Brooks DG. 2021. Opposing roles of type I interferons in cancer immunity. *Annual Review of Pathology* **16**:167–198. DOI: https://doi.org/10.1146/annurev-pathol-031920-093932, PMID: 33264572

Brattain MG, Strobel-Stevens J, Fine D, Webb M, Sarrif AM. 1980. Establishment of mouse colonic carcinoma cell lines with different metastatic properties. *Cancer Research* **40**:2142–2146 PMID: 6992981.

Catarinella M, Monestiroli A, Escobar G, Fiocchi A, Tran NL, Aiolfi R, Marra P, Esposito A, Cipriani F, Aldrighetti L, Iannacone M, Naldini L, Guidotti LG, Sitia G. 2016. Ifnα gene/cell therapy curbs colorectal cancer colonization of the liver by acting on the hepatic microenvironment. *EMBO Molecular Medicine* **8**:155–170. DOI: https://doi.org/10.15252/emmm.201505395, PMID: 26769348

Chambers AF, Groom AC, MacDonald IC. 2002. Dissemination and growth of cancer cells in metastatic sites. *Nature Reviews. Cancer* **2**:563–572. DOI: https://doi.org/10.1038/nrc865, PMID: 12154349

Chen EY, Tan CM, Kou Y, Duan Q, Wang Z, Meirelles GV, Clark NR, Ma'ayan A. 2013. Enrichr: interactive and collaborative HTML5 gene list enrichment analysis tool. *BMC Bioinformatics* **14**:128. DOI: https://doi.org/10.1186/1471-2105-14-128, PMID: 23586463

Chen Y, Lun ATL, Smyth GK. 2016. From reads to genes to pathways: differential expression analysis of RNA-Seq experiments using rsubread and the edger quasi-likelihood pipeline. *F1000Research* **5**:1438. DOI: https://doi.org/10.12688/f1000research.8987.2, PMID: 27508061

Cheon H, Borden EC, Stark GR. 2014. Interferons and their stimulated genes in the tumor microenvironment. *Seminars in Oncology* **41**:156–173. DOI: https://doi.org/10.1053/j.seminoncol.2014.02.002, PMID: 24787290

Chow FC-L, Chok KS-H. 2019. Colorectal liver metastases: an update on multidisciplinary approach. *World Journal of Hepatology* **11**:150–172. DOI: https://doi.org/10.4254/wjh.v11.i2.150, PMID: 30820266

Cogger VC, O'Reilly JN, Warren A, Le Couteur DG. 2015. A standardized method for the analysis of liver sinusoidal endothelial cells and their fenestrations by scanning electron microscopy. *Journal of Visualized Experiments* **e52698**:e52698. DOI: https://doi.org/10.3791/52698, PMID: 25993325

Crist SB, Ghajar CM. 2021. When a house is not a home: a survey of antimetastatic niches and potential mechanisms of disseminated tumor cell suppression. *Annual Review of Pathology* **16**:409–432. DOI: https://doi.org/10.1146/annurev-pathmechdis-012419-032647, PMID: 33276706

Cunningham D, Atkin W, Lenz HJ, Lynch HT, Minsky B, Nordlinger B, Starling N. 2010. Colorectal cancer. *Lancet* **375**:1030–1047. DOI: https://doi.org/10.1016/S0140-6736(10)60353-4, PMID: 20304247

Curtsinger JM, Gerner MY, Lins DC, Mescher MF. 2007. Signal 3 availability limits the CD8 T cell response to a solid tumor. *Journal of Immunology* **178**:6752–6760. DOI: https://doi.org/10.4049/jimmunol.178.11.6752, PMID: 17513722

DeLeve LD. 2015. Liver sinusoidal endothelial cells in hepatic fibrosis. *Hepatology* **61**:1740–1746. DOI: https://doi.org/10.1002/hep.27376, PMID: 25131509

Denève E, Riethdorf S, Ramos J, Nocca D, Coffy A, Daurès JP, Maudelonde T, Fabre JM, Pantel K, Alix-Panabières C. 2013. Capture of viable circulating tumor cells in the liver of colorectal cancer patients. *Clinical Chemistry* **59**:1384–1392. DOI: https://doi.org/10.1373/clinchem.2013.202846, PMID: 23695297

De Palma M, Mazzieri R, Politi LS, Pucci F, Zonari E, Sitia G, Mazzoleni S, Moi D, Venneri MA, Indraccolo S, Falini A, Guidotti LG, Galli R, Naldini L. 2008. Tumor-Targeted interferon-alpha delivery by tie2-expressing monocytes inhibits tumor growth and metastasis. *Cancer Cell* **14**:299–311. DOI: https://doi.org/10.1016/j.ccr.2008.09.004, PMID: 18835032

Dobrzanski MJ, Reome JB, Dutton RW. 2000. Type 1 and type 2 CD8+ effector T cell subpopulations promote long-term tumor immunity and protection to progressively growing tumor. *Journal of Immunology* **164**:916–925. DOI: https://doi.org/10.4049/jimmunol.164.2.916, PMID: 10623840

Efremova M, Rieder D, Klepsch V, Charoentong P, Finotello F, Hackl H, Hermann-Kleiter N, Löwer M, Baier G, Krogsdam A, Trajanoski Z. 2018. Targeting immune checkpoints potentiates immunoediting and changes the dynamics of tumor evolution. *Nature Communications* **9**:32. DOI: https://doi.org/10.1038/s41467-017-02424-0, PMID: 29296022

Engstrand J, Strömberg C, Nilsson H, Freedman J, Jonas E. 2019. Synchronous and metachronous liver metastases in patients with colorectal cancer-towards a clinically relevant definition. *World Journal of Surgical Oncology* **17**:228. DOI: https://doi.org/10.1186/s12957-019-1771-9, PMID: 31878952

Fioravanti J, González I, Medina-Echeverz J, Larrea E, Ardaiz N, González-Aseguinolaza G, Prieto J, Berraondo P. 2011. Anchoring interferon alpha to apolipoprotein A-I reduces hematological toxicity while enhancing immunostimulatory properties. *Hepatology***53**:1864–1873. DOI: https://doi.org/10.1002/hep.24306, PMID: 21425312

Flanigan RC, Salmon SE, Blumenstein BA, Bearman SI, Roy V, McGrath PC, Caton JR Jr, Munshi N, Crawford ED. 2001. Nephrectomy followed by interferon alfa-2b compared with interferon alfa-2b alone for metastatic renal-cell cancer. *The New England Journal of Medicine* **345**:1655–1659. DOI: https://doi.org/10.1056/NEJMoa003013, PMID: 11759643

Foser S, Weyer K, Huber W, Certa U. 2003. Improved biological and transcriptional activity of monopegylated interferon-alpha-2a isomers. *The Pharmacogenomics Journal* **3**:312–319. DOI: https://doi.org/10.1038/sj.tpj.6500204, PMID: 14569259

Franciszkiewicz K, Boissonnas A, Boutet M, Combadière C, Mami-Chouaib F. 2012. Role of chemokines and chemokine receptors in shaping the effector phase of the antitumor immune response. *Cancer Research* **72**:6325–6332. DOI: https://doi.org/10.1158/0008-5472.CAN-12-2027, PMID: 23222302

Fu C, Peng P, Loschko J, Feng L, Pham P, Cui W, Lee KP, Krug AB, Jiang A. 2020. Plasmacytoid dendritic cells cross-prime naive CD8 T cells by transferring antigen to conventional dendritic cells through exosomes. *PNAS* **117**:23730–23741. DOI: https://doi.org/10.1073/pnas.2002345117, PMID: 32879009

Fuertes MB, Woo S-R, Burnett B, Fu Y-X, Gajewski TF. 2013. Type I interferon response and innate immune sensing of cancer. *Trends in Immunology* **34**:67–73. DOI: https://doi.org/10.1016/j.it.2012.10.004, PMID: 23122052

Gerl K, Miquerol L, Todorov VT, Hugo CPM, Adams RH, Kurtz A, Kurt B. 2015. Inducible glomerular erythropoietin production in the adult kidney. *Kidney International* **88**:1345–1355. DOI: https://doi.org/10.1038/ki.2015.274, PMID: 26398496

Gessani S, Conti L, Del Cornò M, Belardelli F. 2014. Type I interferons as regulators of human antigen presenting cell functions. *Toxins* **6**:1696–1723. DOI: https://doi.org/10.3390/toxins6061696, PMID: 24866026

Gissen P, Arias IM. 2015. Structural and functional hepatocyte polarity and liver disease. *Journal of Hepatology* **63**:1023–1037. DOI: https://doi.org/10.1016/j.jhep.2015.06.015, PMID: 26116792

Glinskii OV, Huxley VH, Glinsky GV, Pienta KJ, Raz A, Glinsky VV. 2005. Mechanical entrapment is insufficient and intercellular adhesion is essential for metastatic cell arrest in distant organs. *Neoplasia* **7**:522–527. DOI: https://doi.org/10.1593/neo.04646, PMID: 15967104

Glue P, Rouzier-Panis R, Raffanel C, Sabo R, Gupta SK, Salfi M, Jacobs S, Clement RP, The Hepatitis C Intervention Therapy Group. 2000. A dose-ranging study of pegylated interferon alfa-2b and ribavirin in chronic hepatitis C. *Hepatology* **32**:647–653. DOI: https://doi.org/10.1053/jhep.2000.16661, PMID: 10960463

Guidotti LG, Inverso D, Sironi L, Di Lucia P, Fioravanti J, Ganzer L, Fiocchi A, Vacca M, Aiolfi R, Sammicheli S, Mainetti M, Cataudella T, Raimondi A, Gonzalez-Aseguinolaza G, Protzer U, Ruggeri ZM, Chisari FV, Isogawa M, Sitia G, Iannacone M. 2015. Immunosurveillance of the liver by intravascular effector CD8 (+) T cells. *Cell* **161**:486–500. DOI: https://doi.org/10.1016/j.cell.2015.03.005, PMID: 25892224

Gül N, Bögels M, Grewal S, van der Meer AJ, Rojas LB, Fluitsma DM, van den Tol MP, Hoeben KA, van Marle J, de Vries HE, Beelen RHJ, van Egmond M. 2011. Surgery-Induced reactive oxygen species enhance colon carcinoma cell binding by disrupting the liver endothelial cell lining. *Gut* **60**:1076–1086. DOI: https://doi.org/10.1136/gut.2010.224717, PMID: 21278144

Herndon TM, Demko SG, Jiang X, He K, Gootenberg JE, Cohen MH, Keegan P, Pazdur R. 2012. U.S. food and drug administration approval: peginterferon-alfa-2b for the adjuvant treatment of patients with melanoma. *The Oncologist* **17**:1323–1328. DOI: https://doi.org/10.1634/theoncologist.2012-0123, PMID: 23002124

Horowitz M, Neeman E, Sharon E, Ben-Eliyahu S. 2015. Exploiting the critical perioperative period to improve long-term cancer outcomes. *Nature Reviews. Clinical Oncology* **12**:213–226. DOI: https://doi.org/10.1038/nrclinonc.2014.224, PMID: 25601442

Inagawa R, Okada H, Takemura G, Suzuki K, Takada C, Yano H, Ando Y, Usui T, Hotta Y, Miyazaki N, Tsujimoto A, Zaikokuji R, Matsumoto A, Kawaguchi T, Doi T, Yoshida T, Yoshida S, Kumada K, Ushikoshi H, Toyoda I, et al. 2018. Ultrastructural alteration of pulmonary capillary endothelial glycocalyx during endotoxemia. *Chest* **154**:317–325. DOI: https://doi.org/10.1016/j.chest.2018.03.003, PMID: 29555594

Indraccolo S. 2010. Interferon-Alpha as angiogenesis inhibitor: learning from tumor models. *Autoimmunity* **43**:244–247. DOI: https://doi.org/10.3109/08916930903510963, PMID: 20166871

Jacobs F, Wisse E, De Geest B. 2010. The role of liver sinusoidal cells in hepatocyte-directed gene transfer. *The American Journal of Pathology* **176**:14–21. DOI: https://doi.org/10.2353/ajpath.2010.090136, PMID: 19948827

Jeon S, Juhn JH, Han S, Lee J, Hong T, Paek J, Yim DS. 2013. Saturable human neopterin response to interferon-α assessed by a pharmacokinetic-pharmacodynamic model. *Journal of Translational Medicine* **11**:240. DOI: https://doi.org/10.1186/1479-5876-11-240, PMID: 24088361

Karmaus PWF, Chi H. 2014. Genetic dissection of dendritic cell homeostasis and function: lessons from cell type-specific gene ablation. *Cellular and Molecular Life Sciences* **71**:1893–1906. DOI: https://doi.org/10.1007/s00018-013-1534-7, PMID: 24366237

Katlinski KV, Gui J, Katlinskaya YV, Ortiz A, Chakraborty R, Bhattacharya S, Carbone CJ, Beiting DP, Girondo MA, Peck AR, Puré E, Chatterji P, Rustgi AK, Diehl JA, Koumenis C, Rui H, Fuchs SY. 2017. Inactivation of interferon receptor promotes the establishment of immune privileged tumor microenvironment. *Cancer Cell* **31**:194–207. DOI: https://doi.org/10.1016/j.ccell.2017.01.004, PMID: 28196594

Katz SC, Pillarisetty VG, Bleier JI, Shah AB, DeMatteo RP. 2004. Liver sinusoidal endothelial cells are insufficient to activate T cells. *Journal of Immunology* **173**:230–235. DOI: https://doi.org/10.4049/jimmunol.173.1.230, PMID: 15210779

Klebanoff CA, Gattinoni L, Torabi-Parizi P, Kerstann K, Cardones AR, Finkelstein SE, Palmer DC, Antony PA, Hwang ST, Rosenberg SA, Waldmann TA, Restifo NP. 2005. Central memory self/tumor-reactive CD8+ T cells confer superior antitumor immunity compared with effector memory T cells. *PNAS* **102**:9571–9576. DOI: https://doi.org/10.1073/pnas.0503726102, PMID: 15980149

Köhne CH, Wilke H, Hiddemann W, Bokemeyer C, Lohrmann HP, Bodenstein H, Preiss J, Rauschecker H, Hill H, Kaufer C, Fischer JT, Ohl U, Urbanitz D, Balleisen L, Schmoll HJ. 1997. Phase II evaluation of 5-fluourouracil plus folinic acid and alpha 2b-interferon in metastatic colorectal cancer. *Oncology* **54**:96–101. DOI: https://doi.org/10.1159/000227670, PMID: 9075778

Kondo T, Okabayashi K, Hasegawa H, Tsuruta M, Shigeta K, Kitagawa Y. 2016. The impact of hepatic fibrosis on the incidence of liver metastasis from colorectal cancer. *British Journal of Cancer* **115**:34–39. DOI: https://doi.org/10.1038/bjc.2016.155, PMID: 27280634

Kuleshov MV, Jones MR, Rouillard AD, Fernandez NF, Duan Q, Wang Z, Koplev S, Jenkins SL, Jagodnik KM, Lachmann A, McDermott MG, Monteiro CD, Gundersen GW, Ma'ayan A. 2016. Enrichr: a comprehensive gene set enrichment analysis web server 2016 update. *Nucleic Acids Research* **44**:W90–W97. DOI: https://doi.org/10.1093/nar/gkw377, PMID: 27141961

Lens MB, Dawes M. 2002. Interferon alfa therapy for malignant melanoma: a systematic review of randomized controlled trials. *Journal of Clinical Oncology* **20**:1818–1825. DOI: https://doi.org/10.1200/JCO.2002.07.070, PMID: 11919239

Li Z, Zhu Y, Li C, Trinh R, Ren X, Sun F, Wang Y, Shang P, Wang T, Wang M, Morrison SL, Zhang J. 2017. Anti-VEGFR2-interferon-α2 regulates the tumor microenvironment and exhibits potent antitumor efficacy against colorectal cancer. *Oncoimmunology* **6**:e1290038. DOI: https://doi.org/10.1080/2162402X.2017.1290038, PMID: 28405526

Li G, Zhang Q, Yu Y, Qiu C, Zhang H, Zhang M, Song Z, Yang Y, Hong J, Lu J, Li N, Tang Q, Xu L, Wang X, Zhang W, Chen Z. 2019. Histological responses of peginterferon alpha add-on therapy in patients with chronic hepatitis B with advanced liver fibrosis after long-term nucleos (T) ide analog treatment. *Journal of Viral Hepatitis* **26 Suppl 1**:50–58. DOI: https://doi.org/10.1111/jvh.13152, PMID: 31380590

Liang Y, Tang H, Guo J, Qiu X, Yang Z, Ren Z, Sun Z, Bian Y, Xu L, Xu H, Shen J, Han Y, Dong H, Peng H, Fu YX. 2018. Targeting IFNα to tumor by anti-PD-L1 creates feedforward antitumor responses to overcome checkpoint blockade resistance. *Nature Communications* **9**:4586. DOI: https://doi.org/10.1038/s41467-018-06890-y, PMID: 30389912

Li Destri G, Castaing M, Ferlito F, Minutolo V, Di Cataldo A, Puleo S. 2013. Rare hepatic metastases of colorectal cancer in livers with symptomatic HBV and HCV hepatitis. *Annali Italiani Di Chirurgia* **84**:323–327 PMID: 22722140.

Lin JD, Feng N, Sen A, Balan M, Tseng HC, McElrath C, Smirnov SV, Peng J, Yasukawa LL, Durbin RK, Durbin JE, Greenberg HB, Kotenko SV. 2016. Distinct roles of type I and type III interferons in intestinal immunity to homologous and heterologous rotavirus infections. *PLOS Pathogens* **12**:e1005600. DOI: https://doi.org/10.1371/journal.ppat.1005600, PMID: 27128797

Link K-H, Kornmann M, Staib L, Redenbacher M, Kron M, Beger HG, Study Group Oncology of Gastrointestinal Tumors. 2005. Increase of survival benefit in advanced resectable colon cancer by extent of adjuvant treatment: results of a randomized trial comparing modulation of 5-FU + levamisole with folinic acid or with interferon-alpha. *Annals of Surgery* **242**:178–187. DOI: https://doi.org/10.1097/01.sla.0000171033.65639.a9, PMID: 16041207

Liu W, Hou Y, Chen H, Wei H, Lin W, Li J, Zhang M, He F, Jiang Y. 2011. Sample preparation method for isolation of single-cell types from mouse liver for proteomic studies. *Proteomics* **11**:3556–3564. DOI: https://doi.org/10.1002/pmic.201100157, PMID: 21751380

Love MI, Huber W, Anders S. 2014. Moderated estimation of fold change and dispersion for RNA-Seq data with deseq2. *Genome Biology* **15**:550. DOI: https://doi.org/10.1186/s13059-014-0550-8, PMID: 25516281

Madisen L, Zwingman TA, Sunkin SM, Oh SW, Zariwala HA, Gu H, Ng LL, Palmiter RD, Hawrylycz MJ, Jones AR, Lein ES, Zeng H. 2010. A robust and high-throughput CRE reporting and characterization system for the whole mouse brain. *Nature Neuroscience* **13**:133–140. DOI: https://doi.org/10.1038/nn.2467, PMID: 20023653

Mak KM, Mei R. 2017. Basement membrane type IV collagen and laminin: an overview of their biology and value as fibrosis biomarkers of liver disease. *The Anatomical Record* **300**:1371–1390. DOI: https://doi.org/10.1002/ar.23567, PMID: 28187500

Mitchell MJ, King MR. 2014. Physical biology in cancer. 3. the role of cell glycocalyx in vascular transport of circulating tumor cells. *American Journal of Physiology-Cell Physiology* **306**:C89–C97. DOI: https://doi.org/10.1152/ajpcell.00285.2013, PMID: 24133067

Montoya M, Schiavoni G, Mattei F, Gresser I, Belardelli F, Borrow P, Tough DF. 2002. Type I interferons produced by dendritic cells promote their phenotypic and functional activation. *Blood* **99**:3263–3271. DOI: https://doi.org/10.1182/blood.v99.9.3263, PMID: 11964292

Offeddu GS, Hajal C, Foley CR, Wan Z, Ibrahim L, Coughlin MF, Kamm RD. 2021. The cancer glycocalyx mediates intravascular adhesion and extravasation during metastatic dissemination. *Communications Biology* **4**:255. DOI: https://doi.org/10.1038/s42003-021-01774-2, PMID: 33637851

Pandey E, Nour AS, Harris EN. 2020. Prominent receptors of liver sinusoidal endothelial cells in liver homeostasis and disease. *Frontiers in Physiology* **11**:873. DOI: https://doi.org/10.3389/fphys.2020.00873, PMID: 32848838

Park CG, Hartl CA, Schmid D, Carmona EM, Kim HJ, Goldberg MS. 2018. Extended release of perioperative immunotherapy prevents tumor recurrence and eliminates metastases. *Science Translational Medicine* **10**:eaar1916. DOI: https://doi.org/10.1126/scitranslmed.aar1916, PMID: 29563317

Pavlović Ž, Risović D, Novaković D. 2012. Comparative study of direct and indirect image-based profilometry in characterization of surface roughness. *Surface and Interface Analysis* **44**:825–830. DOI: https://doi.org/10.1002/sia.4889

Postic C, Shiota M, Niswender KD, Jetton TL, Chen Y, Moates JM, Shelton KD, Lindner J, Cherrington AD, Magnuson MA. 1999. Dual roles for glucokinase in glucose homeostasis as determined by liver and pancreatic beta cell-specific gene knock-outs using Cre recombinase. *The Journal of Biological Chemistry* **274**:305–315. DOI: https://doi.org/10.1074/jbc.274.1.305, PMID: 9867845

Poynard T, McHutchison J, Manns M, Trepo C, Lindsay K, Goodman Z, Ling MH, Albrecht J. 2002. Impact of pegylated interferon alfa-2b and ribavirin on liver fibrosis in patients with chronic hepatitis C. *Gastroenterology* **122**:1303–1313. DOI: https://doi.org/10.1053/gast.2002.33023, PMID: 11984517

Prigge JR, Hoyt TR, Dobrinen E, Capecchi MR, Schmidt EE, Meissner N. 2015. Type I IFNs act upon hematopoietic progenitors to protect and maintain hematopoiesis during Pneumocystis lung infection in mice. *Journal of Immunology* **195**:5347–5357. DOI: https://doi.org/10.4049/jimmunol.1501553, PMID: 26519535

Reitsma S, Slaaf DW, Vink H, van Zandvoort MAMJ, oude Egbrink MGA. 2007. The endothelial glycocalyx: composition, functions, and visualization. *Pflugers Archiv* **454**:345–359. DOI: https://doi.org/10.1007/s00424-007-0212-8, PMID: 17256154

Rodriguez A, Regnault A, Kleijmeer M, Ricciardi-Castagnoli P, Amigorena S. 1999. Selective transport of internalized antigens to the cytosol for MHC class I presentation in dendritic cells. *Nature Cell Biology* **1**:362–368. DOI: https://doi.org/10.1038/14058, PMID: 10559964

Rosenberg SA, Spiess P, Lafreniere R. 1986. A new approach to the adoptive immunotherapy of cancer with tumor-infiltrating lymphocytes. Science **233**:1318–1321. DOI: https://doi.org/10.1126/science.3489291, PMID: 3489291

Sallusto F, Geginat J, Lanzavecchia A. 2004. Central memory and effector memory T cell subsets: function, generation, and maintenance. *Annual Review of Immunology* **22**:745–763. DOI: https://doi.org/10.1146/annurev.immunol.22.012703.104702, PMID: 15032595

Sargent D, Sobrero A, Grothey A, O'Connell MJ, Buyse M, Andre T, Zheng Y, Green E, Labianca R, O'Callaghan C, Seitz JF, Francini G, Haller D, Yothers G, Goldberg R, de Gramont A. 2009. Evidence for cure by adjuvant therapy in colon cancer: observations based on individual patient data from 20,898 patients on 18 randomized trials. *Journal of Clinical Oncology* **27**:872–877. DOI: https://doi.org/10.1200/JCO.2008.19.5362, PMID: 19124803

Schindelin J, Arganda-Carreras I, Frise E, Kaynig V, Longair M, Pietzsch T, Preibisch S, Rueden C, Saalfeld S, Schmid B, Tinevez J-Y, White DJ, Hartenstein V, Eliceiri K, Tomancak P, Cardona A. 2012. Fiji: an open-source platform for biological-image analysis. *Nature Methods* **9**:676–682. DOI: https://doi.org/10.1038/nmeth.2019, PMID: 22743772

Schreiber G. 2017. The molecular basis for differential type I interferon signaling. *The Journal of Biological Chemistry* **292**:7285–7294. DOI: https://doi.org/10.1074/jbc.R116.774562, PMID: 28289098

Seo SI, Lim SB, Yoon YS, Kim CW, Yu CS, Kim TW, Kim JH, Kim JC. 2013. Comparison of recurrence patterns between ≤5 years and > 5 years after curative operations in colorectal cancer patients. *Journal of Surgical Oncology* **108**:9–13. DOI: https://doi.org/10.1002/jso.23349, PMID: 23754582

Sitia G, Iannacone M, Aiolfi R, Isogawa M, van Rooijen N, Scozzesi C, Bianchi ME, von Andrian UH, Chisari FV, Guidotti LG. 2011. Kupffer cells hasten resolution of liver immunopathology in mouse models of viral hepatitis. *PLOS Pathogens* **7**:e1002061. DOI: https://doi.org/10.1371/journal.ppat.1002061, PMID: 21655107

Sitia G, Aiolfi R, Di Lucia P, Mainetti M, Fiocchi A, Mingozzi F, Esposito A, Ruggeri ZM, Chisari FV, Iannacone M, Guidotti LG. 2012. Antiplatelet therapy prevents hepatocellular carcinoma and improves survival in a mouse model of chronic hepatitis B. *PNAS* **109**:E2165–E2172. DOI: https://doi.org/10.1073/pnas.1209182109, PMID: 22753481

Sorensen KK, Smedsrod B. 2020. The liver sinusoidal endothelial cell: basic biology and pathobiology. SorensenKK (Ed). *The Liver: Biology and Pathobiology*. Sixth. John Wiley & Sons Ltd. p. 422–434.

Stewart SA, Domínguez-Robles J, Donnelly RF, Larrañeta E. 2018. Implantable polymeric drug delivery devices: classification, manufacture, materials, and clinical applications. *Polymers* **10**:E1379. DOI: https://doi.org/10.3390/polym10121379, PMID: 30961303

Stone JD, Chervin AS, Kranz DM. 2009. T-Cell receptor binding affinities and kinetics: impact on T-cell activity and specificity. *Immunology* **126**:165–176. DOI: https://doi.org/10.1111/j.1365-2567.2008.03015.x, PMID: 19125887

Su T, Yang Y, Lai S, Jeong J, Jung Y, McConnell M, Utsumi T, Iwakiri Y. 2021. Single-Cell transcriptomics reveals zone-specific alterations of liver sinusoidal endothelial cells in cirrhosis. *Cellular and Molecular*

Gastroenterology and Hepatology **11**:1139–1161. DOI: https://doi.org/10.1016/j.jcmgh.2020.12.007, PMID: 33340713

Subramanian A, Tamayo P, Mootha VK, Mukherjee S, Ebert BL, Gillette MA, Paulovich A, Pomeroy SL, Golub TR, Lander ES, Mesirov JP. 2005. Gene set enrichment analysis: a knowledge-based approach for interpreting genome-wide expression profiles. *PNAS* **102**:15545–15550. DOI: https://doi.org/10.1073/pnas.0506580102, PMID: 16199517

Sung H, Ferlay J, Siegel RL, Laversanne M, Soerjomataram I, Jemal A, Bray F. 2021. Global cancer statistics 2020: GLOBOCAN estimates of incidence and mortality worldwide for 36 cancers in 185 countries. *CA* **71**:209–249. DOI: https://doi.org/10.3322/caac.21660

Talamini L, Picchetti P, Ferreira LM, Sitia G, Russo L, Violatto MB, Travaglini L, Fernandez Alarcon J, Righelli L, Bigini P, De Cola L. 2021. Organosilica cages target hepatic sinusoidal endothelial cells avoiding macrophage filtering. *ACS Nano* **15**:9701–9716. DOI: https://doi.org/10.1021/acsnano.1c00316

Tanjore H, Kalluri R. 2006. The role of type IV collagen and basement membranes in cancer progression and metastasis. *The American Journal of Pathology* **168**:715–717. DOI: https://doi.org/10.2353/ajpath.2006.051321, PMID: 16507886

Tauriello DVF, Palomo-Ponce S, Stork D, Berenguer-Llergo A, Badia-Ramentol J, Iglesias M, Sevillano M, Ibiza S, Cañellas A, Hernando-Momblona X, Byrom D, Matarin JA, Calon A, Rivas EI, Nebreda AR, Riera A, Attolini CS-O, Batlle E. 2018. Tgfβ drives immune evasion in genetically reconstituted colon cancer metastasis. *Nature* **554**:538–543. DOI: https://doi.org/10.1038/nature25492, PMID: 29443964

Tirone M, Tran NL, Ceriotti C, Gorzanelli A, Canepari M, Bottinelli R, Raucci A, Di Maggio S, Santiago C, Mellado M, Saclier M, François S, Careccia G, He M, De Marchis F, Conti V, Ben Larbi S, Cuvellier S, Casalgrandi M, Preti A, et al. 2018. High mobility group box 1 orchestrates tissue regeneration via CXCR4. *The Journal of Experimental Medicine* **215**:303–318. DOI: https://doi.org/10.1084/jem.20160217, PMID: 29203538

Toyoshima Y, Kitamura H, Xiang H, Ohno Y, Homma S, Kawamura H, Takahashi N, Kamiyama T, Tanino M, Taketomi A. 2019. Il6 modulates the immune status of the tumor microenvironment to facilitate metastatic colonization of colorectal cancer cells. *Cancer Immunology Research* **7**:1944–1957. DOI: https://doi.org/10.1158/2326-6066.CIR-18-0766, PMID: 31554639

Valastyan S, Weinberg RA. 2011. Tumor metastasis: molecular insights and evolving paradigms. *Cell* **147**:275–292. DOI: https://doi.org/10.1016/j.cell.2011.09.024, PMID: 22000009

van der Bij GJ, Bögels M, Otten MA, Oosterling SJ, Kuppen PJ, Meijer S, Beelen RHJ, van Egmond M. 2010. Experimentally induced liver metastases from colorectal cancer can be prevented by mononuclear phagocyte-mediated monoclonal antibody therapy. *Journal of Hepatology* **53**:677–685. DOI: https://doi.org/10.1016/j.jhep.2010.04.023, PMID: 20619916

van Gestel YRBM, de Hingh IHJT, van Herk-Sukel MPP, van Erning FN, Beerepoot LV, Wijsman JH, Slooter GD, Rutten HJT, Creemers G-JM, Lemmens VEPP. 2014. Patterns of metachronous metastases after curative treatment of colorectal cancer. *Cancer Epidemiology* **38**:448–454. DOI: https://doi.org/10.1016/j.canep.2014.04.004, PMID: 24841870

Wang Y, Nakayama M, Pitulescu ME, Schmidt TS, Bochenek ML, Sakakibara A, Adams S, Davy A, Deutsch U, Lüthi U, Barberis A, Benjamin LE, Mäkinen T, Nobes CD, Adams RH. 2010. Ephrin-B2 controls VEGF-induced angiogenesis and lymphangiogenesis. *Nature* **465**:483–486. DOI: https://doi.org/10.1038/nature09002, PMID: 20445537

Warren A, Bertolino P, Benseler V, Fraser R, McCaughan GW, Le Couteur DG. 2007. Marked changes of the hepatic sinusoid in a transgenic mouse model of acute immune-mediated hepatitis. *Journal of Hepatology* **46**:239–246. DOI: https://doi.org/10.1016/j.jhep.2006.08.022, PMID: 17125874

Weber JS, Yang JC, Atkins MB, Disis ML. 2015. Toxicities of immunotherapy for the practitioner. *Journal of Clinical Oncology* **33**:2092–2099. DOI: https://doi.org/10.1200/JCO.2014.60.0379, PMID: 25918278

Wilkinson AL, Qurashi M, Shetty S. 2020. The role of sinusoidal endothelial cells in the axis of inflammation and cancer within the liver. *Frontiers in Physiology* **11**:990. DOI: https://doi.org/10.3389/fphys.2020.00990, PMID: 32982772

Winkler M, Staniczek T, Kürschner SW, Schmid CD, Schönhaber H, Cordero J, Kessler L, Mathes A, Sticht C, Neßling M, Uvarovskii A, Anders S, Zhang X-J, von Figura G, Hartmann D, Mogler C, Dobreva G, Schledzewski K, Géraud C, Koch P-S, et al. 2021. Endothelial GATA4 controls liver fibrosis and regeneration by preventing a pathogenic switch in angiocrine signaling. *Journal of Hepatology* **74**:380–393. DOI: https://doi.org/10.1016/j.jhep.2020.08.033, PMID: 32916216

Wohlfeil SA, Häfele V, Dietsch B, Schledzewski K, Winkler M, Zierow J, Leibing T, Mohammadi MM, Heineke J, Sticht C, Olsavszky V, Koch P-S, Géraud C, Goerdt S. 2019. Hepatic endothelial Notch activation protects against liver metastasis by regulating endothelial-tumor cell adhesion independent of angiocrine signaling. *Cancer Research* **79**:598–610. DOI: https://doi.org/10.1158/0008-5472.CAN-18-1752, PMID: 30530502

Wolf MJ, Hoos A, Bauer J, Boettcher S, Knust M, Weber A, Simonavicius N, Schneider C, Lang M, Stürzl M, Croner RS, Konrad A, Manz MG, Moch H, Aguzzi A, van Loo G, Pasparakis M, Prinz M, Borsig L, Heikenwalder M. 2012. Endothelial CCR2 signaling induced by colon carcinoma cells enables extravasation via the Jak2-Stat5 and p38MAPK pathway. *Cancer Cell* **22**:91–105. DOI: https://doi.org/10.1016/j.ccr.2012.05.023, PMID: 22789541

Yang X, Zhang X, Fu ML, Weichselbaum RR, Gajewski TF, Guo Y, Fu YX. 2014. Targeting the tumor microenvironment with interferon-β bridges innate and adaptive immune responses. *Cancer Cell* **25**:37–48. DOI: https://doi.org/10.1016/j.ccr.2013.12.004, PMID: 24434209

Yu X, Chen L, Liu J, Dai B, Xu G, Shen G, Luo Q, Zhang Z. 2019. Immune modulation of liver sinusoidal endothelial cells by melittin nanoparticles suppresses liver metastasis. *Nature Communications* **10**:574. DOI: https://doi.org/10.1038/s41467-019-08538-x, PMID: 30718511

Yun S, Huang JJ. 2016. Routes for drug delivery: sustained-release devices. *Developments in Ophthalmology* **55**:84–92. DOI: https://doi.org/10.1159/000434692, PMID: 26501913

Zhang Y, Davis C, Ryan J, Janney C, Peña MMO. 2013. Development and characterization of a reliable mouse model of colorectal cancer metastasis to the liver. *Clinical & Experimental Metastasis* **30**:903–918. DOI: https://doi.org/10.1007/s10585-013-9591-8, PMID: 23748471

Appendix 1

Appendix 1—key resources table

Reagent type (species) or resource	Designation	Source or reference	Identifiers	Additional information
Strain, strain background (*Mus musculus*)	C57BL/6 J	Charles River, Italy	Strain code: 632	Inbred
Strain, strain background (*Mus musculus*)	BALB/c	Charles River Lab	Strain code: 028	Inbred
Strain, strain background (*Mus musculus*)	NSG (NOD.Cg-Prkdcscid Il2rgtm1Wjl/SzJ)	Charles River Lab	Strain code: 614	Immun odeficient
Strain, strain background (*Mus musculus*)	*Ifnar1*$^{fl/fl}$ (B6(Cg)-*Ifnar1*tm1.1Ees/J)	Jackson Lab	*JAX:028256*	C57BL/6 J background
Strain, strain background (*Mus musculus*)	*Alb*^{Cre} (B6.Cg-Speer6-ps1Tg(*Alb*-cre)21Mgn/J)	Jackson Lab	JAX:003574	C57BL/6 J background
Strain, strain background (*Mus musculus*)	*Pdgfrb*^{CreERT2} (B6.Cg-Tg(Pdgfrb-cre/ERT2)6096Rha/J)	Jackson Lab	JAX:029684	C57BL/6 J background
Strain, strain background (*Mus musculus*)	*Itgax*^{Cre} (CD11c, B6.Cg-Tg(*Itgax*-cre)1-1Reiz/J)	Jackson Lab	JAX:008068	C57BL/6 J background
Strain, strain background (*Mus musculus*)	Rosa26-ZsGreen (B6.Cg-Gt(ROSA)26Sortm6(CAG-ZsGreen1)Hze/J)	Jackson Lab	JAX:007906	C57BL/6 J background
Strain, strain background (*Mus musculus*)	*VeCad*^{CreERT2} (*Cdh5*(PAC)$^{-CreERT2}$ mice)	Taconic, Models for life	Provided by S. Brunelli (UniMib, Milan)	C57BL/6 J background
Strain, strain background (*Mus musculus*)	OT-I mice (C57BL/6-Tg(TcraTcrb) 1100Mgb/Crl)	Charles River Lab	JAX:003831	C57BL/6 J background
Antibody	Anti-CD126, IL-6RA, (clone: D7715A7) (Rat monoclonal)	Biolegend	Cat# 115806, RRID:AB_313676	FC (1:100)
Antibody	anti-CD18, ITGB2 (clone M18/2) (Rat monoclonal)	Biolegend	Cat# 101402, RRID:AB_312811	FC (1:100)
Antibody	Anti-CD49d, ITGA4, (clone 9C10(MFR4.B)) (Rat monoclonal)	Biolegend	Cat# 103706, RRID:AB_313046	FC (1:100)
Antibody	Anti-H-2K^{b}/H-2D^{b} (clone 28-8-6) (Mouse monoclonal)	Biolegend	Cat# 114605, RRID:AB_313596	FC (1:100)
Antibody	Anti-CD86 (clone GL-1) (Rat monoclonal)	Biolegend	Cat# 105007, RRID:AB_313150	FC (1:100)
Antibody	Anti-CD146 (clone ME-9F1) (Rat monoclonal)	Biolegend	Cat# 134704, RRID:AB_2143527	FC (1:100)
Antibody	Anti-CD44 (clone IM7) (Rat monoclonal)	Biolegend	Cat# 103044, RRID:AB_2650923	FC (1:100)
Antibody	Anti-CD62L (clone MEL-14) (Rat monoclonal)	Biolegend	Cat# 104420, RRID:AB_493376	FC (1:100)
Antibody	Anti- CD16/CD32, (Rat monoclonal)	BioXCell	Cat# BE0307; RRID:AB_2736987	FC (1:100)
Antibody	Anti-GFP, (Rabbit polyclonal)	Thermo Fisher Sci	Cat# A11122, RRID:AB_221569	IF (1:100)
Antibody	Anti-GFP (clone FM264G) (Rat monoclonal)	Biolegend	Cat# 338008, RRID:AB_2563288	IF (1:100)
Antibody	Anti-CD31, PECAM1, (Goat polyclonal)	R&D Systems	Cat# AF3628, RRID:AB_2161028	IF (1:300)

Appendix 1 Continued on next page

Appendix 1 Continued

Reagent type (species) or resource	Designation	Source or reference	Identifiers	Additional information
Antibody	Anti-PDGFRβ, CD140b (clone APB5) (Rat monoclonal)	eBioscience	Cat# 14-1402-82, RRID:AB_467493	IF (1:200)
Antibody	Anti-CD11c, (clone N418) (Armenian hamster monoclonal)	Biolegend	Cat#117312, RRID:AB_492850	IF (1:100)
Antibody	Anti-Heparan Sulfate (clone F58-10E4) (Mouse monoclonal)	Amsbio	Cat# 370255 S, RRID:AB_10891554	IF (1:50)
Antibody	Anti-LYVE-1 (Rabbit polyclonal)	Novus Biol	Cat# NB600-1008, RRID:AB_10000497	IF (1:300)
Antibody	Anti-Collagen type IV (Rabbit polyclonal)	Abcam	Cat# ab19808, RRID:AB_445160	IF (1:100)
Antibody	Anti-Laminin (Rabbit polyclonal)	Sigma-Aldrich	Cat# L9393, RRID:AB_477163	IF (1:300)
Antibody	Anti-CD54, ICAM1 (clone YN1/1.7.4) (Rat monoclonal)	Biolegend	Cat#116101, RRID:AB_313692	IF (1:100)
Antibody	Anti-CD62E, E-selectin (clone 10E9.6) (Rat monoclonal)	BD Bioscience	Cat#550290, RRID:AB_393585	IF (1:100)
Antibody	Anti-Rabbit AF488 (Donkey polyclonal)	Thermo Fisher Sci	Cat#32790, RRID:AB_2762833	IF (1:200)
Antibody	Anti-Goat AF546 (Donkey polyclonal)	Thermo Fisher Sci	Cat#A-11056, RRID:AB_2534103	IF (1:200)
Antibody	Anti-Rat AF647 (Donkey polyclonal)	Jackson IR	Cat#712-605-153, RRID:AB_2340694	IF (1:200)
Antibody	Anti-IgM conjugated to APC (clone II/41) (Rat monoclonal)	Thermo Fisher Sci	Cat#17-5790-82, RRID:AB_469458	IF (1:100)
Antibody	Anti-Ki-67 (clone SP6) (Rabbit recombinant antibody)	Thermo Fisher Sci	Cat# MA5-14520, RID:AB_10979488	IHC (1:200)
Antibody	Anti-CD34 (clone MEC14.7) (Rat monoclonal)	Biolegend	Cat# 119301, RRID:AB_345279	IHC (1:300)
Antibody	Anti-F4/80 (clone A3-1) (Rat monoclonal)	Bio-Rad	Cat# MCA497, RRID:AB_2098196	IHC (1:200)
Antibody	Anti-CD3 (clone SP7) (Rabbit monoclonal)	Abcam	Cat# ab21703, RRID:AB_446487	IHC (1:100)
Antibody	Anti-pSTAT1 (Clone 58D6) (Rabbit monoclonal)	Cell Signaling	Cat# BK9167S, RRID:AB_561284	IHC (1:800)
Antibody	Anti-CD11c microbeads ultrapure	Miltenyi Biotec	Cat# 130-125-835	100 µL per 10^8 total cells
Antibody	Anti-F4/80 microbeads ultrapure	Miltenyi Biotec	Cat# 130-110-443	100 µL per 10^8 total cells
Antibody	InVivoMAb Anti-mouse GM-CSF(clone MP1-22E9) (Rat monoclonal)	BioXcell	Cat# BE0259 RRID:AB_2687738	40 ng/ml
Peptide, recombinant protein	Recombinant mouse IFNα1, carrier-free	Biolegend	Cat# 751802	
Peptide, recombinant protein	NH2-SIINFEKL-COOH (SL-8 peptide)	Proimmune	Cat# GMPT5995	
Chemical compound, drug	Albumin from chicken egg white (ovalbumin)	Sigma-Aldrich	Cat# 55039	
Chemical compound, drug	Gadoxetic acid (Primovist; Gd-EOB-DTPA)	Bayer Schering Pharma	N/A	

Appendix 1 Continued on next page

Appendix 1 Continued

Reagent type (species) or resource	Designation	Source or reference	Identifiers	Additional information
Chemical compound, drug	Tamoxifen	Sigma Aldrich	Cat# T5648-5G	
Chemical compound, drug	Lipofectamine 2000	Thermo Fisher Sci	Cat# 11668019	
Chemical compound, drug	Paraformaldehyde powder	Sigma-Aldrich	Cat# 158127	
Chemical compound, drug	Sodium Cacodylate powder	Sigma-Aldrich	Cat# C0250	
Chemical compound, drug	25% EM grade Glutaraldehyde	ProSciTech	Cat# C001	
Chemical compound, drug	Osmium tetroxide	ProSciTech	Cat# C011	
Chemical compound, drug	Lanthanum (III) nitrate hexahydrate	MERK	Cat# 331937–11 G	2%
Chemical compound, drug	Zinc formalin fixative	Sigma-Aldrich	Cat# Z2902-3.75L	
Chemical compound, drug	Fibronectin human plasma	MERK	Cat# F2006-1MG	
Chemical compound, drug	Percoll	Sigma-Aldrich	Cat# P4937-500ML	
Chemical compound, drug	Matrigel Matrix	BD Bioscience	Cat# 354248	
Chemical compound	7-AAD Viability staining solution	Biolegend	Cat# 420404	FC (1:100)
Chemical compound, drug	EGM-2MV endothelial cell growth medium-2 BulletKit	Lonza	Cat# CC-3202	
Chemical compound, drug	Brefeldin A	Sigma-Aldrich	Cat# B7651	
Commercial assay, kit	VeriKine-HS Mouse IFNα All-Subtype ELISA Kit	PBL Assay Sci	Cat# 42115–1	
Commercial assay, kit	GeneArt CRISPR Nuclease Vector with OFP Reporter Kit	Thermo Fisher Sci	Cat# A21174	
Commercial assay, kit	TOPO TA Cloning Kit	Thermo Fisher Sci	Cat# 450641	
Commercial assay, kit	CellTiter-Glo Luminescent Cell Viability Assay	Promega	Cat# G7570	
Commercial assay, kit	ReliaPrep RNA Cell Miniprep System	Promega	Cat# Z6011	
Commercial assay, kit	ReliaPrep RNA Tissue Miniprep System	Promega	Cat# Z6111	
Commercial assay, kit	TURBO DNA-free kit	Ambion	Cat# AM1907	
Commercial assay, kit	QIAamp DNA Mini kit	Qiagen	Cat# 51304	
Commercial assay, kit	RNeasy Mini Kit	Qiagen	Cat# 74104	
Commercial assay, kit	Procyte kit	Idexx	Cat# 9926306–00	
Commercial assay, kit	Live/Dead fixable near-IR dead cell stain kit	Thermo Fisher Sci	Cat# L34975	FC (1:500)
Commercial assay, kit	Live/Dead fixable Green dead cell stain kit	Thermo Fisher Sci	Cat# L34970	FC (1:100)
Commercial assay, kit	DNAse TURBO	Thermo Fisher Sci	Cat# AM1907	

Appendix 1 Continued on next page

Appendix 1 Continued

Reagent type (species) or resource	Designation	Source or reference	Identifiers	Additional information
Commercial assay, kit	Foxp3/Transcription Factor Staining buffer set	Thermo Fisher Sci	Cat# 00-5523-00	
Cell lines (*Mus musculus*)	CT26	ATCC	Cat# CRL-2638, RID:CVCL_7256	
Cell lines (*Mus musculus*)	MC38	Kindly provided by P. Berraondo López - Centro de Investigación Médica Aplicada (Spain)	RRID:CVCL_B288	
Sequence-based reagent	*Ifnar1* intron 3 forward	***Prigge et al., 2015***	PCR primers	ACTCAGGTTCG CTCCATCAG
Sequence-based reagent	*Ifnar1* intron 3 reverse	***Prigge et al., 2015***	PCR primers	GCACATTGACCATT ACAAGAGTAG
Sequence-based reagent	*Ifnar1* exon2 forward	This paper	PCR primers	TCCAAGACTCC TGCTGTC
Sequence-based reagent	*Ifnar1* exon2 reverse	This paper	PCR primers	GCACTTTTAC TTGCTCGGT
Sequence-based reagent	*Itgax*^{Cre} forward	Jackson Lab	PCR primers	ACTTGGCAGCTG TCTCCAAG
Sequence-based reagent	*Itgax*^{Cre} reverse	Jackson Lab	PCR primers	GTGGCAGATGG CGCGGCA
Sequence-based reagent	*ALB*^{Cre} forward	Jackson Lab	PCR primers	CCAGGCTAAGTGCC TTCTCTACA
Sequence-based reagent	*ALB*^{Cre} reverse	Jackson Lab	PCR primers	AATGCTTCTGTCC GTTTGCCGGT
Sequence-based reagent	*PdgfrbCre* forward	Jackson Lab	PCR primers	GAACTGTCACC GGGAGGA
Sequence-based reagent	*PdgfrbCre* reverse	Jackson Lab	PCR primers	AGGCAAATTTT GGTGTACGG
Sequence-based reagent	*VeCad*^{Cre} forward	***Wang et al., 2010***	PCR primers	GCCTGCATTACCG GTCGATGCAACG
Sequence-based reagent	*VeCad*^{Cre} reverse	***Wang et al., 2010***	PCR primers	GTGGCAGATGGCG CGGCAACACCAT
Sequence-based reagent	RosaZsgreen forward	Jackson Lab	PCR primers	AACCAGAAGTGG CACCTGAC
Sequence-based reagent	RosaZsgreen reverse	Jackson Lab	PCR primers	GGCATTAAAGC AGCGTATCC
Sequence-based reagent	crRNA1	Thermo Fisher Sci	CRISPR RNA guide	TAGACGTCTATATT CTCAGGGTTTT
Sequence-based reagent	crRNA2	Thermo Fisher Sci	CRISPR RNA guide	ATGTAGACGTCTAT ATTCTCGTTTT
Sequence-based reagent	Mm00516793_g1	Thermo Fisher Sci	Taqman probe *Irf7*	
Sequence-based reagent	Mm00836412_m1	Thermo Fisher Sci	Taqman probe *Oas1*	
Sequence-based reagent	Mm 99999915_g1	Thermo Fisher Sci	Taqman probe *Gapdh*	
Software and algorithms	FlowJo v10.5 or greater	Tree Star	RRID:SCR_008520	
Software and algorithms	Prism version 8 or greater	GraphPad	RRID:SCR_002798	
Software and algorithms	ImageScope software	Leica Biosystems	RRID:SCR_014311	
Software and algorithms	Imaris version 7.2.3	Bitplane	RRID:SCR_007370;	
Software and algorithms	Fiji software or ImageJ software	NIH	RRID:SCR_002285; 003070	

Appendix 1 Continued on next page

Appendix 1 Continued

Reagent type (species) or resource	Designation	Source or reference	Identifiers	Additional information
Software and algorithms	MIPAV v5.3.4 or greater	CIT, NIH	RRID:SCR_007371	
Software and algorithms	EsivisionPro 3.2 software	Soft Imaging Sys	N/A	
Software and algorithms	OsiriX DICOM viewer version 3.9.2 or greater	Pixmeo SARL	N/A	
Software and algorithms	Trimmomatic version 0.32	***Bolger et al., 2014***	RRID:SCR_011848	
Software and algorithms	STAR aligner version 2.5.3 a	STAR SRL	RRID:SCR_004463	
Software and algorithms	GENECODE version M22	Ensmbl 97	N/A	
Software and algorithms	R-4.0.3 software	R Core Team	N/A	
Software and algorithms	DESeq2 version 1.30.1	***Love et al., 2014***	N/A	
Software and algorithms	EnrichR R package version 3.3	***Chen et al., 2013***	RRID:SCR_020938	
Software and algorithms	GeneArt CRISPR Search and Design Tool	Thermo Fisher Sci	N/A	
Other	Alzet osmotic pumps 1002	Alzet	Cat# 10104844	Mini osmotic pump (MOP)
Other	Alzet osmotic pumps 1004	Alzet	Cat# 10104846	Mini osmotic pump (MOP)
Other	ProCyte Dx Hematology Analyzer	IDEXX Lab	N/A	Instruments
Other	Bruker Horizontal 7-Tesla MRI scanner	BioSpec	N/A	Instruments
Other	ViiA7 Fast Real-Time PCR System	Applied Biosys	Cat# 4453543	Instruments
Other	Aperio Scanscope XT Leica	Leica Biosystems	RRID:SCR_018457	Instruments
Other	Leica SP8 LIGHTNING confocal microscope	Leica Biosystems	RRID:SCR_018169	Instruments
Other	FEI Talos L120C G2 Transmission electron microscope	Thermo Fisher Sci	N/A	Instruments
Other	Zeiss FEG Gemini 500 Scanning electron microscope	Zeiss	N/A	Instruments
Other	FACSCanto II High Throughput Sampler	BD Bioscience	N/A	Instruments
Other	FACS LSRFortessa	BD Bioscience	N/A	Instruments
Other	FACSAria Fusion	BD Bioscience	N/A	Instruments
Other	Illumina NovaSeq 6000 machine	Illumina	RRID:SCR_016387	Instruments
Other	Leica CM1520 Cryostat	Leica Biosystems	RRID:SCR_017543	Instruments
Other	Leica VT1000S Vibratome	Leica Biosystems	RRID:SCR_016495	Instruments
Other	EM UC7 ultramicrotome	Leica Biosystems	RRID:SCR_016694	Instruments